The CBETA Fractional Arc Test

Cornell-Brookhaven ERL Test Accelerator

CBETA Note 032

Principle Investigators: G. Hoffstaetter and D. Trbojevic

Editor: C. Gulliford

Contributors: N. Banerjee, J. Barley, A. Bartnik, I. Bazarov, I. Ben-Zvi, J. S. Berg, S. Brooks, D. Burke, J. Crittenden, J. Dobbins, R. Gallagher, B. Heltsley, R. Hulsart, J. Jones, D. Jusic, R. Kaplan, D. Kelliher, V. Kostroun, B. Kuske, Y. Li, M. Liepe, W. Lou, G. Mahler, M. McAteer, F. Méot, R. Michnoff, M. Minty, R. Patterson, S. Peggs, V. Ptitsyn, P. Quigley, T. Roser, D. Sabol, D. Sagan, J. Sears, K. Smolenski, E. Smith, S. Trabocchi, J. Tuozzolo, N. Tsoupas, V. Veshcherevich, J. Vöelker, D. Widger

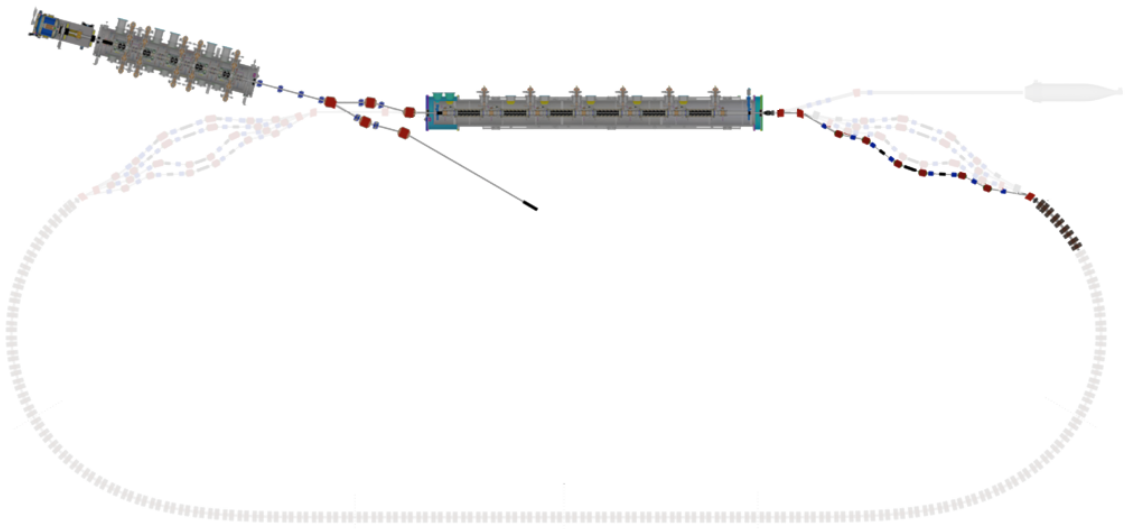

September 2018

Contents

1 Introduction

The construction of a high energy, high luminosity, polarized Electron-Ion Collider (EIC) remains one of the highest priorities for the nuclear physics and accelerator communities and continues to drive research and development of many state-of-the-art accelerator technologies [1, 2]. These include (but are not limited to): high-brightness, high current electron sources capable of delivering both polarized and unpolarized electrons, various electron-ion cooling schemes, as well as (multi-pass) Energy Recovery Linacs (ERL). In fact, both the electron - Relativistic Heavy Ion Collider (eRHIC) under design at Brookhaven National Lab (BNL), and the Jefferson lab Electron-Ion Collider (JLEIC) under design at Thomas Jefferson National Accelerator Facility (TJNAF) require high current electron beams for use in electron ion cooling, making the use of an ERL design attractive [3]. Both designs require significant development of the underlying accelerator technologies, as well as investigation of possible cost reducing schemes. In the case of the eRHIC design(s), the use of Fixed Field Alternating-gradient (FFA) recirculating loop(s) may provide significant cost reduction by reducing both the length of the linac, and the number of recirculating loops required.

As part of this development effort, the Cornell-BNL Energy recovery linac Test Accelerator (CBETA) [3], a 4-pass, 150 MeV energy recovery linac (ERL), utilizing a Non-scaling Fixed Field Alternating-gradient (NS-FFA) permanent magnet return loop, is currently under design and construction at Cornell University through the joint collaboration of Brookhaven National Lab (BNL) and the Cornell Laboratory for Accelerator based Sciences and Education (CLASSE). Building on the significant advancements in high-brightness photoelectron sources and SRF technology at Cornell [4–9], as well as the FFA magnet and lattice design expertise from BNL, CBETA will establish the operation of a multi-turn SRF based ERL utilizing a compact FFA return loop with large energy acceptance (a factor of roughly 3.6 in energy), and thus demonstrate one possible cost-reduction technology under consideration for the eRHIC design. Moreover, successful completion of the CBETA project requires the study and measurement of many critical phenomena relevant to designing the EIC: the Beam-Breakup (BBU) instability, halo-development and collimation, growth in energy spread from Coherent Synchrotron Radiation (CSR), and CSR micro bunching, and thus should provide valuable insight to the EIC and ERL communities [3].

In order to demonstrate the viability of the CBETA design, the Fractional Arc Test (FAT) was added to the CBETA commissioning sequence. Completed in the spring of 2018, this test brought together for the first time elements of all of the critical subsystems required for the CBETA project: the injector, the Main Linac Cryomodule (MLC), the low energy (first) splitter line which includes several new electromagnets, a path length adjustment mechanism, and a new BPM system, as well as a first prototype production permanent magnet girder featuring 4 cells of the FFA return loop with its own corresponding vacuum system and BPM design. Consequently, the main technical goals of the FAT included: recommissioning of the injector, full energy commissioning of the main linac with beam, commissioning of the S1

splitter line including beam-based calibration of the S1 magnets and diagnostics, testing of the splitter path length adjustment mechanism, calibration of the S1 and FA BPM designs, and beam based characterization of the permanent magnets in the Fractional FA arc. Fig. 1.0.1 shows the first 42 MeV beam passed through the entire FAT beamline to the viewscreen just after the FFA section. While in some sense symbolic in nature, the taking of this image

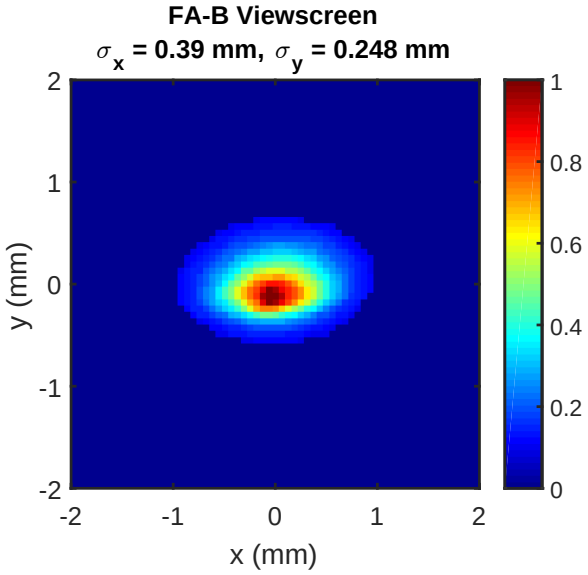

Figure 1.0.1: First measured transverse beam profile for a 42 MeV beam on the last viewscreen after the fractional arc section.

represented a major milestone for the FAT experiment, as well as the CBETA project as a whole. The remainder of this work describes in detail both the beam measurements performed, as well as the measurements and experience gained operating the main linac with beam at full energy during the FAT commissioning period. This description begins with a discussion of the FAT experimental layout.

1.1 Experimental Set-up

Construction of the CBETA machine at Cornell began in earnest with the disassembling and removal of the injector [4–7, 10] from its original experimental hall in early 2015. At this time, the Injector Crymodule (ICM) was temporarily removed for maintenance, and a short beamline constructed to study high current operation (up to 45 mA) from the original Cornell DC gun in the CBETA experimental hall. Between 2016-2017, after the maintenance on the ICM was completed, the injector was rebuilt and recommissioned, now with the Cornell Mark II DC gun, which features a segmented insulator design [11–13]. Additionally, during that time the Main Linac Cryomodule was installed and tested without beam [9] in the CBETA experimental hall before being moved to its final location for CBETA. Finally, installation of the lowest energy splitter line and the fractional FFA arc were completed in early 2018 in

anticipation for beam tests that spring.

1.1.1 Layout

Together, Fig. 1.1.1 and 1.1.2 show the beamline layout of the CBETA fractional arc test (FAT). In particular Fig. 1.1.1 shows the Cornell injector, merger section, diagnostic beamline, and Main Linac Cryomodule (MLC). For these measurements, the Cornell DC gun used in this layout was high voltage processed up to roughly 350 kV using similar procedures as described in [11]. However, given the limited number of photocathodes currently available for the CBETA project, the gun voltage was limited to 300 kV for all measurements in this work to ensure no photocathode damage occurring from occasional vacuum activity when operating at higher voltages. The photocathode used exclusively in this work was a NaKSb cathode with roughly 4.5% QE. Grown on a polished steel puck, this cathode is very similar to the one used previously in the injector to set the record for highest average current from a photoinjector [4]. While the MTE of this cathode was not measured directly, similarly grown cathodes in the past typically have MTE around 140 meV. The drive laser used in conjunction with this cathode is the same 50 MHz, 520 nm laser system [14] used previously for low emittance/high bunch charge measurements [5–7]. This laser produces roughly 1 ps long pulses, which are shaped longitudinally using four rotatable birefringent crystals set to produce a roughly flat-top distribution with a 9.3 ps RMS duration. The use of a pulse picking Pockels cell following this pulse shaping allows further reduction of the average beam power. Typical operation would create pulse trains between 0.3-1.0 microseconds long, at rates from 0.3-2.0 KHz.

In the FAT, much of the injector layout following the gun remains the same as described before [5]: the beam is compressed transversely and longitudinally using a normal conducting 1.3 GHz bunching cavity and two emittance compensation solenoids located in the beamline immediately after the gun (labeled as "A1"), before being accelerated to the CBETA injection energy of 6 MeV in the injector cryomodule (ICM). Following the ICM the beam is passed through a four-quad telescope ("A3") and a merger section comprised of a conventional three-dipole achromat ("B1"), and matched into the linac ("D1"). For characterization of the injector beam and to verify this matching, the FAT layout features a diagnostic beamline line ("B2") comprised of a separate merger mirroring the merger into the linac, followed by suite of diagnostics including the Cornell injector emittance measurement system (EMS). The placement of the EMS at roughly the corresponding position of the first MLC cavity allows for detailed characterization of the beam entering the MLC. The EMS installed here makes use of the same two-slit direct phase space measurement system described in detail in [15, 16], and features a vertical deflecting cavity [17] for time resolution of the vertical phase space. Following the EMS is dipole spectrometer, which combined with the deflecting cavity allows for the direct measurement of the longitudinal phase space of the beam.

Beams sent to the linac nominally receive a total of 36 MeV from the combined voltage of the six 7-cell 1.3 GHz SRF cavities of the MLC before being passed into the CBETA low energy splitter line (labeled "S1"). Through the settings on its 8 dipoles and 8 quadrupole magnets, the S1 splitter line will prepare the beam's parameters $\{x, y, x', y', \alpha_{x,y}, \beta_{x,y}, \eta_x, \eta'_x, r_{56}\}$ to the values needed in the FFA. In addition, through the use of path length adjustment stages and bellows, the length of the S1 line is tunable in order to correctly time the return of the beam for energy recovery in future CBETA experiments.

The fractional FFA arc is a prototype example of the first arc girder for CBETA. The magnets are all Halbach style permanent magnets of two types, a focusing quadarupole and a defocusing gradient dipole. It begins with a half-length defocusing magnet, and then four cells of the periodic FFA arc lattice, each of which consists of a focusing and a defocusing magnet in a doublet configuration. There are four BPMs throughout the girder in periodic positions centered in the shorter drift of the cell, all of which were instrumented for the FAT, and four total viewscreens: two viewscreens within the arc (centered in the long drifts between cells 1 and 2, and 3 and 4), and one viewscreen at both the entrance and exit to the arc. The horizontal and vertical corrector dipoles that are wound around the permanent quadrupole magnets were installed but not powered during the FAT test.

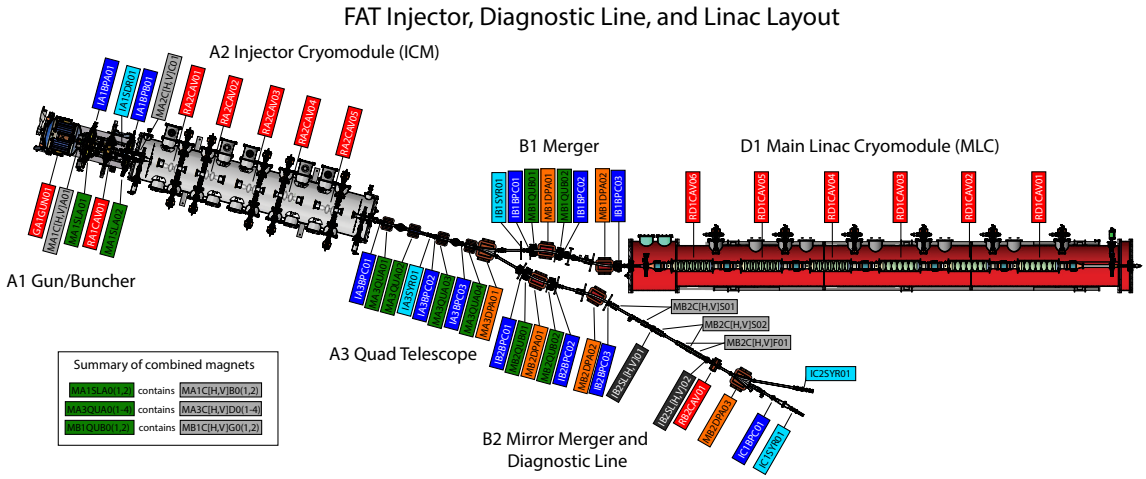

Figure 1.1.1: Layout of the injector, merger, linac, and diagnostic sections of the FAT experiment. The beam begins in the gun section ("A1"), accelerates to 6 MeV in the Injector Cryomodule ("A2"), and then merges into the Main Linac Cryomodule ("B1", "D1").

1.1.2 Modeling

The majority of the CBETA lattice design was done using BMAD, primarily within the Tao simulation environment [18, 19]. In order to avoid complications from space charge, the design lattice begins after the MLC, where the beam has reached a sufficiently high energy that space charge can be safely neglected. This allows the simulation to be calculated quickly, but then adds the complication that the beam's initial Twiss parameters after the MLC are undetermined. So, the Twiss parameters at that point were allowed to be free parameters, and eventually chosen to best complement the rest of the CBETA lattice.

Modeling from the cathode up to that Twiss matching point was performed in General Particle Tracer (GPT) [20, 21] in order to include effects from space charge and has been well documented in previous work [5], including details of the user interface connecting the injector EPICS control system to the space charge simulations.

For online simulation of the single particle dynamics, we developed a new online model,

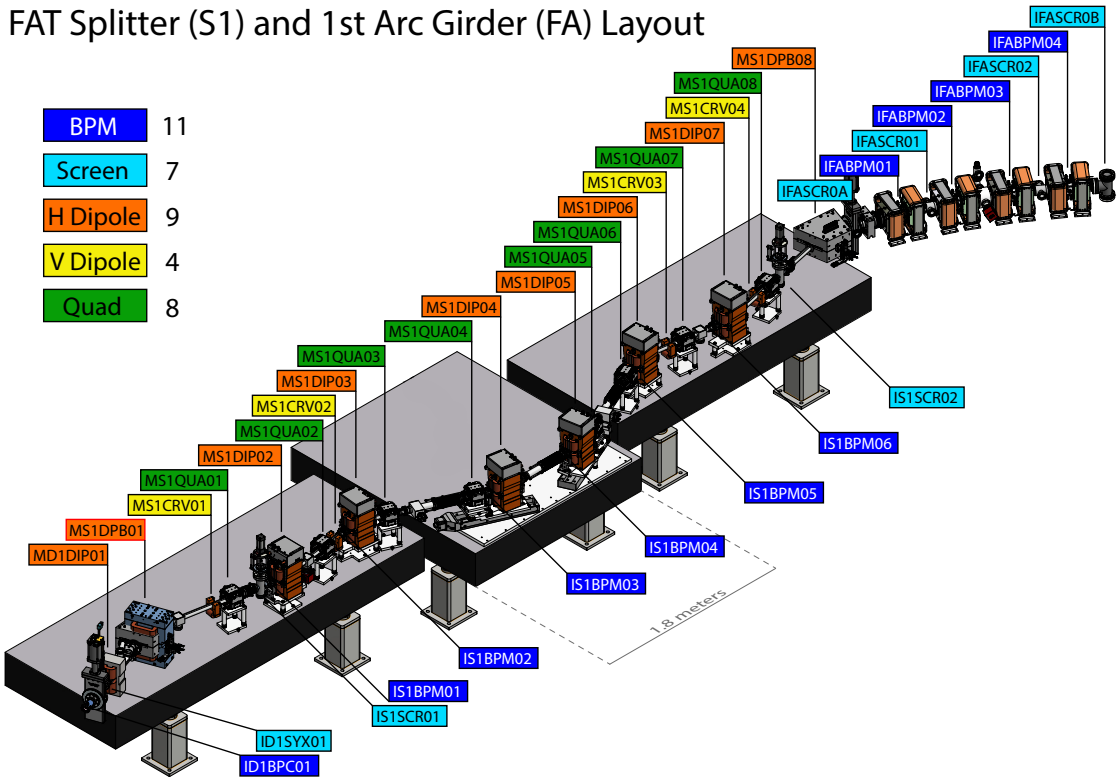

Figure 1.1.2: Layout of the post linac section of the FAT experiment. Beam exits the linac and enters the S1 splitter line at the bottom right and proceeds to the fractional FA arc (top right).

called the CBETA Virtual Machine which combines the functionality of the TAO environment with the ability to communicate with EPICS [22]. When running, this software creates its own copy of the CBETA EPICS control system, allowing users to command the virtual optical elements in the simulation via standard EPICS commands. By changing any of the element strengths in the model, the software computes all relevant single particle tracking data (i.e. centroid orbit, dispersion, transfer matrix, etc), and publishes the results to its own additional EPICS records, thus making the virtual machine data available to the user via EPICS in exactly the same manner as real machine data. This allows for any automated measurement procedure to command and take data from either/both the real and virtual machine, and thus provides both the ability to easily produce simulated predictions of measured data, as well as realistic debugging of automated measurement procedures. Many of the experimental procedures used in this work were developed and tested offline in this manner. The software also provides a "sync" mode where the Virtual Machine continuously monitors the status of real, and updates the simulated machine data upon detecting a change in the settings of the real machine, thus providing a useful online diagnostic as well. For the low energy portion of the FAT layout (injector through MLC), the CBETA Virtual Machine uses similar fieldmap data similar to corresponding maps used in the corresponding GPT lattice described above. While necessary for capturing the low energy dynamics, tracking through field maps inevitably slows down the simulation, and leads to simulation times of on the order of a few seconds, making the results near real time.

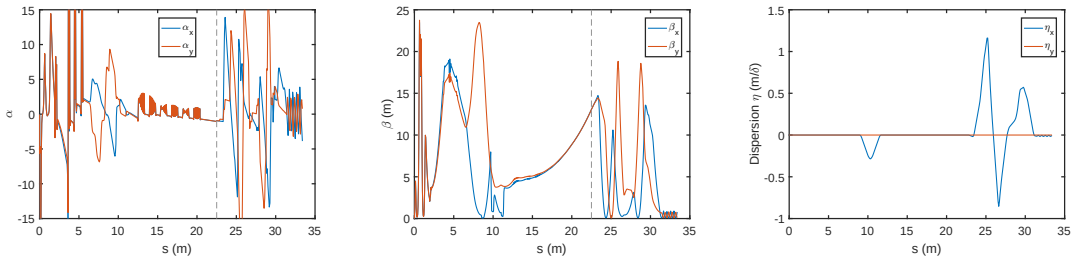

(a) GPT (left of dashed line) and BMAD (right of dashed line) predictions for α.

(b) GPT (left side) and BMAD (right side) predictions for β.

(c) BMAD prediction for the dispersion η.

Figure 1.1.3: Nominal simulated Twiss parameters: beam dynamics with space charge are simulated up to $s = 22.5$ m (just after the linac) using GPT. The resulting beam distribution is then tracked using BMAD to end of the fractional arc. The dashed line in (a) and (b) shows the point where the two simulations are joined. In the plot of dispersion, only the BMAD simulation is shown for all s.

Many of the experimental procedures used in this work were developed and tested offline in this manner. The software also provides a "sync" mode where the Virtual Machine continuously monitors the status of real, and updates the simulated machine data upon detecting a change in the settings of the real machine, thus providing a useful online diagnostic as well. For the low energy portion of thet FAT layout (injector through MLC), the CBETA Virtual Machine uses similar fieldmap data similar to corresponding maps used in the corresponding

GPT lattice described above. While necessary for capturing the low energy dynamics, tracking through field maps inevitably slows down the simulation, and leads to simulation times of on the order of a few seconds, making the results near real time.

Bibliography

[1] Aprahamian, A. *et al. Reaching for the horizon: The 2015 long range plan for nuclear science* (2015).

[2] National Academies of Sciences, E. and Medicine. *An Assessment of U.S.-Based Electron-Ion Collider Science*. The National Academies Press, Washington, DC (2018). ISBN 978-0-309-47856-4. doi:10.17226/25171.

[3] Hoffstaetter, G. H., *et al. CBETA Design Report, Cornell-BNL ERL Test Accelerator*. ArXiv e-prints (June 2017).

[4] Dunham, B., *et al. Record high-average current from a high-brightness photoinjector*. Applied Physics Letters, **102** (3), 034105 (2013). doi:10.1063/1.4789395.

[5] Gulliford, C., *et al. Demonstration of low emittance in the Cornell energy recovery linac injector prototype*. Phys. Rev. ST Accel. Beams, **16**, page 073401 (Jul 2013). doi:10.1103/PhysRevSTAB.16.073401.

[6] Gulliford, C., *et al. Demonstration of cathode emittance dominated high bunch charge beams in a DC gun-based photoinjector*. Applied Physics Letters, **106** (9), 094101 (2015). doi:http://dx.doi.org/10.1063/1.4913678.

[7] Bartnik, A., *et al. Operational experience with nanocoulomb bunch charges in the Cornell photoinjector*. Phys. Rev. ST Accel. Beams, **18**, page 083401 (Aug 2015). doi:10.1103/PhysRevSTAB.18.083401.

[8] Eichhorn, R., *et al. The Cornell Main Linac Cryomodule: A Full Scale, High Q Accelerator Module for cw Application*. Physics Procedia, **67**, pages 785 – 790 (2015). ISSN 1875-3892. doi:https://doi.org/10.1016/j.phpro.2015.06.133. Proceedings of the 25th International Cryogenic Engineering Conference and International Cryogenic Materials Conference 2014.

[9] (2016). Proceedings of the North American Particle Accelerator Conference.

[10] Full, S., *et al. Detection and clearing of trapped ions in the high current Cornell photoinjector*. Phys. Rev. Accel. Beams, **19**, page 034201 (Mar 2016). doi:10.1103/PhysRevAccelBeams.19.034201.

[11] Maxson, J., *et al. Design, conditioning, and performance of a high voltage, high brightness dc photoelectron gun with variable gap*. Review of Scientific Instruments, **85** (9), 093306 (2014). doi:http://dx.doi.org/10.1063/1.4895641.

[12] Maxson, J., *et al. Measurement of the tradeoff between intrinsic emittance and quantum efficiency from a NaKSb photocathode near threshold.* Applied Physics Letters, **106** (23), 234102 (2015). doi:http://dx.doi.org/10.1063/1.4922146.

[13] Maxson, J., *et al. Adaptive Electron Beam Shaping Using a Photoemission Gun and Spatial Light Modulator.* submitted to Phys. Rev. ST Accel. Beams (2014).

[14] Zhao, Z., *et al. High-power fiber lasers for photocathode electron injectors.* Phys. Rev. ST Accel. Beams, **17**, page 053501 (May 2014). doi:10.1103/PhysRevSTAB.17.053501.

[15] Bazarov, I. V., *et al. Benchmarking of 3D space charge codes using direct phase space measurements from photoemission high voltage dc gun.* Phys. Rev. ST Accel. Beams, **11**, page 100703 (Oct 2008). doi:10.1103/PhysRevSTAB.11.100703.

[16] Li, H. *Mutli-dimensional Characterization of the Laser and Electron Beams of the Cornell Energy Recovery Linac Photoinjector Prototype.* Ph.D. thesis, Cornell University (August 2012).

[17] Belomestnykh, S., *et al. Deflecting cavity for beam diagnostics at Cornell ERL injector.* Nuclear Instruments and Methods in Physics Research Section A: Accelerators, Spectrometers, Detectors and Associated Equipment, **614** (2), pages 179 – 183 (2010). ISSN 0168-9002. doi:10.1016/j.nima.2009.12.063.

[18] Urban, J., L. Fields, and D. Sagan. *Linear Accelerator Simulations with Bmad.* In *Proceedings of the 2005 Particle Accelerator Conference*, pages 1937–1939 (May 2005). ISSN 1944-4680. doi:10.1109/PAC.2005.1590964.

[19] Sagan, D. and J. C. Smith. *The TAO Accelerator Simulation Program.* In *Proceedings of the 2005 Particle Accelerator Conference*, pages 4159–4161 (May 2005). ISSN 1944-4680. doi:10.1109/PAC.2005.1591750.

[20] *Pulsar Website for GPT.* http://www.pulsar.nl/gpt/ (2011).

[21] van der Geer, S., *et al. Institute of Physics Conference Series.* 175, page 101 (2005).

[22] https://epics.anl.gov/.

2 Beam Commissioning

As previously stated, the FAT provided the first opportunity for systematic beam commissioning of many of the critical CBETA accelerator and instrumentation subsystems. The most important include: full energy commissioning of the MLC with beam, commissioning of the S1 splitter line including beam-based calibration of the S1 magnets and diagnostics, and testing of the splitter path length adjustment mechanism, as well as calibration of the FA BPM design and characterization of the permanent magnets in the Fractional FA arc. Consequently, the measurements completed during the FAT break down naturally into the following categories: tune-up and characterization of the injector at 6 MeV, beam calibration of the MLC cavities, tune-up and characterization of the beam dynamics in the S1 splitter line and FFA fractional arc at the nominal 42 MeV settings, and finally characterization of the beam dynamics through the S1 line and FFA fractional arc over a wide energy range (specifically 38.5 - 59 MeV). In conjunction with beam measurements, use of the CBETA-V virtual machine allowed for both on and offline verification of BMAD model of the FAT experiment, as well as development and testing of related control systems software.

2.1 Injector Tune-up and Characterization

Ultimately, the demonstration of the CBETA design parameters hinges on the production and transport of high quality beams in the injector. For bunch charges within the design bunch charge range of 0-125 pC, space charge forces dominate the dynamics of the beam throughout the injector (and to a lesser extent through the first pass of the linac), and thus require detailed modeling and optimization to ensure emittance preservation and proper matching into the main linac. For this work, we made use of the same Multi-Objective Genetic Algorithm optimization (MOGA) software used in [1–5], and applied it to 3D space charge simulations of the beam passing through injector, merger, and MLC.

To ensure the highest beam quality and proper matching of the beam at the end of the MLC and entering the S1 splitter, the optimizer minimized the emittance at the match point (s = 22.5 m) as a function of the maximum error in the match to the desired four Twiss parameters $\beta_{x,y}$ = 12.5 m, and $\alpha_{x,y} = -1$ for several different bunch charges ranging up to 125 pC. Table-2.1.1 displays an example of the resulting optimized injector settings for a 6 pC bunch charge. We note that while the design Twiss values are specified at the end of the MLC, their only direct measurement is located in the EMS in the diagnostic line, which is equivalent to a measurement at the entrance to the first MLC cavity, not at the optimized match point.

We began injector tuning by loading the machine settings from the 6 pC GPT simulation into the machine, and then manual tuning from that starting point. The procedure involved first measuring both the horizontal and vertical phase spaces of the beam using the EMS, calculating the Twiss parameters from the measured distributions, and then manually adjusting

Table 2.1.1: Simulated and Experimental Injector Settings

Name	Simulation	Experiment	Units
Bunch charge	6	6	pC
Laser diameter (rms)	0.28	0.28	mm
Laser duration (rms)	9.3	9.3	ps
Gun voltage	300	300	kV
Solenoid 1 current	-3.07	-3.15	A
Buncher voltage	30	30	kV
Buncher phase	-90	-90	deg.
Solenoid 2 current	2.27	2.28	A
ICM 1 voltage	1500	1500	kV
ICM 1 phase	0	0	deg.
ICM 2 voltage	N/A	N/A	kV
ICM 2 phase	N/A	N/A	deg.
ICM 3 voltage	1600	1600	kV
ICM 3 phase	-15	-15	deg.
ICM 4 voltage	1300	1300	kV
ICM 4 phase	20	20	deg.
ICM 5 voltage	1300	1300	kV
ICM 5 phase	-20	-20	deg.
A3 Quad 1 current	2.30	1.7	A
A3 Quad 2 current	1.21	1.0	A
A3 Quad 3 current	-2.54	-1.8	A
A3 Quad 4 current	-1.86	-1.8	A
B1 Quad 1 current	6.0	6.0	A
B1 Quad 2 current	6.0	6.0	A

machine parameters (primarily the quadrupoles in the A3 section and the solenoids in the A1 section) to try to optimize them. After we reached an acceptable machine setting, we re-ran GPT using the measured initial laser distribution and the used machine settings. Comparison between the measured and simulated phase spaces are shown in Fig. 2.1.1, and their predicted Twiss functions in Fig. 2.1.2. In addition, we also measured the beam size on all viewscreens throughout the injector at this machine setting, and summarized that data in Fig. 2.1.2. In general, the data shows strong qualitative agreement and near quantitative agreement. Perhaps most interesting is the skew in the measured transverse profile of the beam at the EMS slits. The origin of this remains unresolved, but could be due to tilt errors in the alignment of the quadrupoles in the A3 section. Better agreement with simulation will likely require resolving this problem.

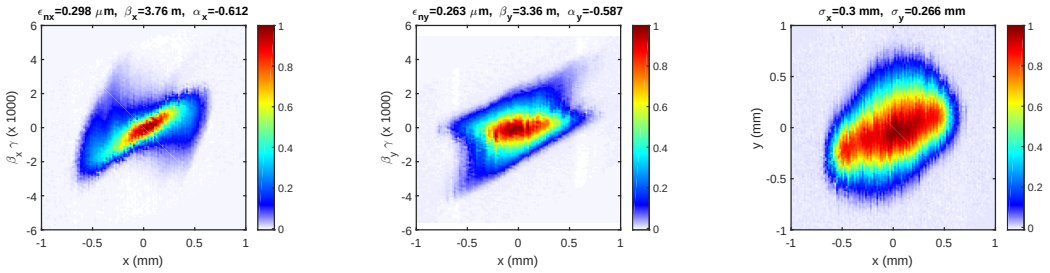

(a) Measured horizontal phase space. (b) Measured vertical phase space. (c) Measured transverse profile.

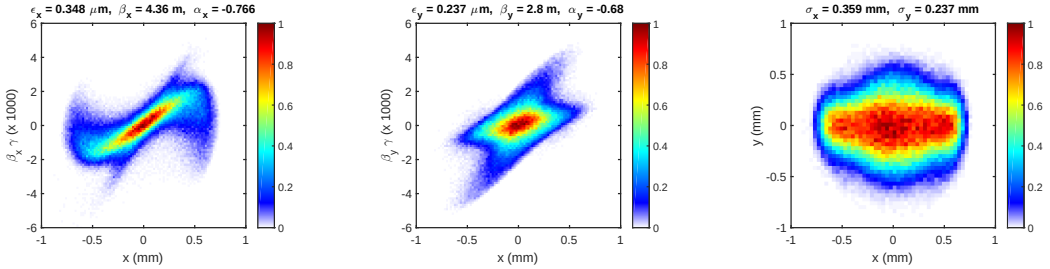

(d) Simulated horizontal phase space. (e) Simulated vertical phase space. (f) Simulated transverse profile.

Figure 2.1.1: Measured (top row) and simulated (bottom row) transverse phase spaces and beam profiles.

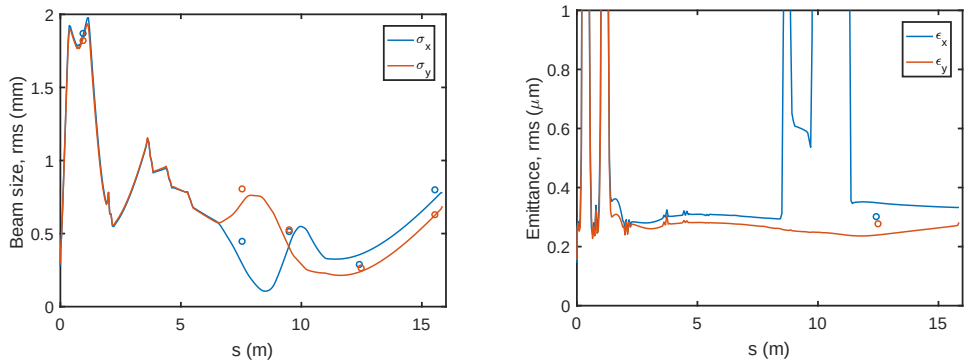

(a) Simulated (lines) and measured (points) rms beam width.

(b) Simulated (lines) and measured (points) rms beam emittance.

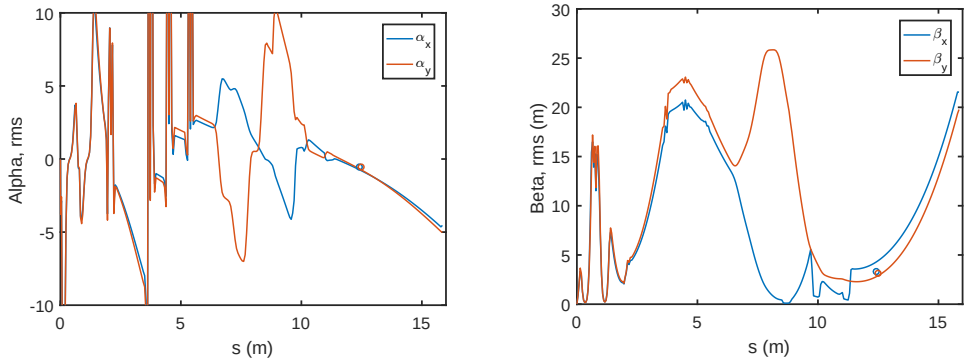

(c) Simulated (lines) and measured (points) alpha.

(d) Simulated (lines) and measured (points) beta.

Figure 2.1.2: Comparison between simulated (lines) and measured (points) properties of the beam through the injector and diagnostic line. The rms beam widths were measured on both viewscreens and in the EMS, while the other plots only show measured data from the EMS (at $s \approx 12.5$). Importantly, the GPT simulations shown here are taken through the diagnostic line, or equivalently, with the MLC turned off, which is why they disagree qualitatively with Fig. 1.1.3 after $s \approx 12.5$ m.

2.2 Main Linac Beam Commissioning

2.2.1 MLC Cavity Energy Gain Calibration and Phasing

Multiple methods were considered for determining the absolute energy gain calibrations of each MLC cavity. For example, a simple spectrometer consisting of a dipole immediately downstream of the MLC followed by a BPM allows for an accurate determination of the beam momentum, provided the spectrometer calibration is known (either by careful analysis of the dipole field or through an initial calibration measurement at a well known beam momentum).

Unfortunately, the FAT layout features a sector magnet just after the MLC. Use of a sector magnet as a spectrometer requires control of the beam orbit entering the dipole, as the integrated field through the magnet depends on the incoming beam position. This is difficult in the FAT layout as there is only a single BPM before this magnet. As an alternative, we opted to use the change in beam arrival phase on the first BPM after the MLC (ID1BPC01) as a measure of energy via the beam's average velocity.

In general, the phase on the BPM downstream of the cavity is given by

$$\phi = \frac{\omega}{c} \int_{\text{cav}}^{\text{bpm}} \frac{ds}{\beta(V_c, \phi_b, E_0)} + \phi_{\text{offset}}, \tag{2.2.1}$$

where $\beta = \beta(s)$ is the velocity of the beam along the trajectory from cavity to BPM determined by the cavity voltage V_c (defined as the on-crest energy gain of a speed of light particle), phase relative to the beam ϕ_b, and initial beam energy E_0. The term ϕ_{offset} represents an unknown BPM specific offset. In this expression, the path length differential depends on the beam's instantaneous transverse angles with respect to the beamline axis: $ds = dz\sqrt{(1 + x'^2 + y'^2)}$. Note that the beam pipe aperture effectively limits the size of the angle terms. Assuming a $2''$ pipe diameter and minimum drift length from the last cavity to the BPM of roughly 2 meters effectively limits the angle terms to roughly $x' \lesssim 25$ mrad. This implies that the correction to the beam phase from the angle terms is on the order of $\delta\phi(x') \lesssim 10^{-3}$. For a (maximum) beam phase change of 360^{o} this corresponds to a correction of about 0.36^{o}, which is within noise level of the BPM phase reading (0.3^{o} for nominal operation), and justifies the approximation $ds \approx dz$. Forming the phase change with respect to the on-crest beam arrival phase gives:

$$\Delta\phi \;=\; \frac{\omega}{c} \int_{\text{cav}}^{\text{bpm}} dz \left(\frac{1}{\beta(V_c, \phi_b)} - \frac{1}{\beta(V_c, \phi_b = 0)} \right), \tag{2.2.2}$$

In general, accurate evaluation of this expression requires particle tracking through the MLC cavity fieldmap (scaled for a desired cavity voltage and phase) and correct drift length from cavity to BPM.

Fig. 2.2.1 shows the phase change computed numerically as a function of cavity voltage V_c and beam phase ϕ_b for a 6 MeV beam entering the first (RD1CAV06) and last cavity (RD1CAV01), respectively. While not shown, similar results for the other MLC cavities demonstrate that the phase change accurately scales with the distance from cavity to BPM. For the examples shown, this implies that the data in Fig. 2.2.1b should be approximately given by scaling the data in Fig. 2.2.1a by roughly 9/2, which one can see holds true by examining the maximum in the each plot.

Inversion of Eq. (2.2.2) in the least squares sense provides a simple way of determining the cavity energy gain calibration V_c, as well as the initial beam energy entering the cavity E_0 (if not known), from the measured BPM phase change $\Delta\phi$ for each cavity. The two cavity parameters V_c and ϕ_b in this expression suggest two methods for changing the energy gain through each cavity and thus the BPM $\Delta\phi$ for fitting: ramping up the cavity voltage at constant phase, or changing the cavity phase at constant voltage. The voltage scan method suffers from the fact that it implies knowledge of the beam phase ϕ_b at each cavity setting,

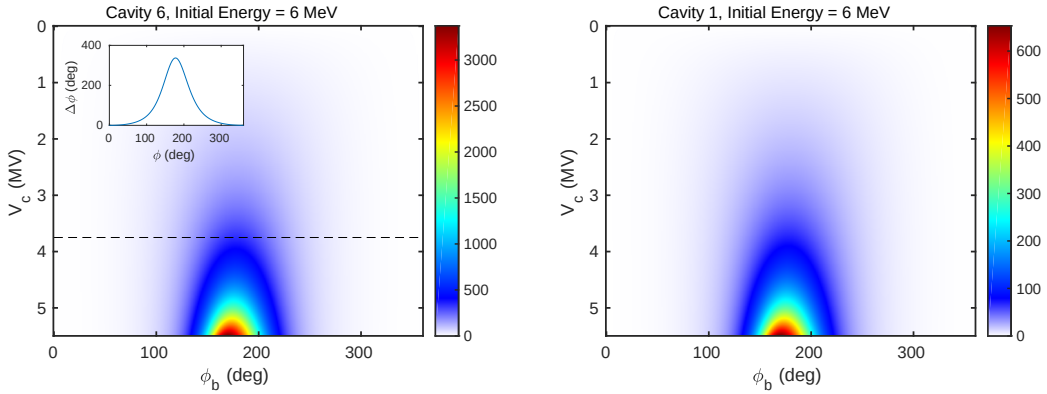

(a) First cavity (RD2CAV06) phase shift. (b) Last cavity (RD2CAV01) phase shift.

Figure 2.2.1: Relative BPM phase change $\Delta\phi$ as a function of both cavity phase and cavity energy gain for the first cavity (a) and last cavity (b). The dashed line and inset shown in (a) display the voltage and *predicted* phase change used in calibrating the first MLC cavity.

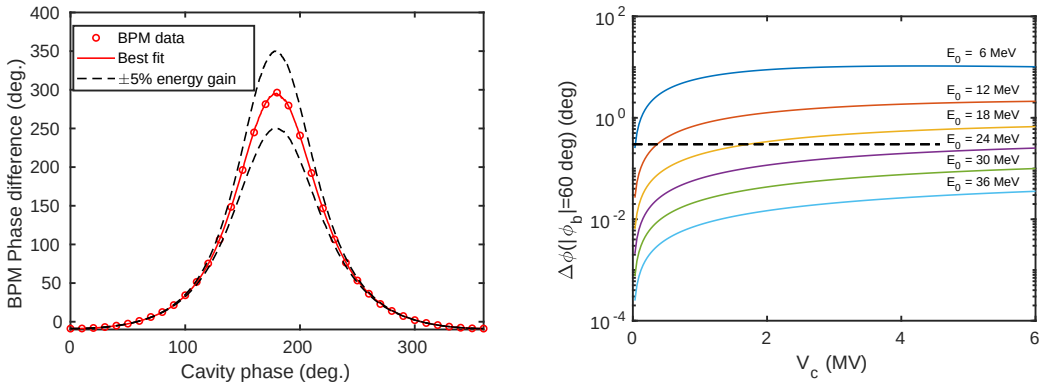

(a) First cavity (RD2CAV06) phase shift. (b) Phase change for cavity phasing.

Figure 2.2.2: Change of the arrival time of the beam (shown as a phase change with respect to the RF clock) as a function of MLC cavity 6 phase set-point at a constant cavity gradient. Measured points are shown compared to the best fit model, and models that have ±5% energy gain. Right: Change of the arrival time of the beam (shown as a phase change with respect to the RF clock) for each MLC cavity voltage turned on sequentially. The input energy to the cavity being scanned assumes the cavities before it are set to the nominal 6 MV voltage.

while the phase scan method requires no knowledge of ϕ_b (the on-crest phase is found by including it as another fit parameter) and still provides significant measured phase change,

particularly when decelerating the beam. After settling on this method, each MLC cavity was calibrated by first setting the voltage to a fixed value of roughly 2-4 MeV, and then slowly changing the cavity phase from 0-360°. An example set of data for the first MLC cavity is shown in Fig. 2.2.2a. In the figure, the trend for the best fit energy calibration is shown, along with energy gains 5% higher and lower, to give a sense of the measurement sensitivity. From the random error in the BPM phases, we estimate an error of approximately 0.4% for the final cavity calibrations. Assuming this represents the most significant source of error, this implies an overall error in the total MLC energy gain of roughly $\sqrt{6} \cdot 0.4\% \approx 1\%$ for any given machine setting.

In addition to the cavity energy gain calibrations, use of the beam arrival phase in principle allows for the determination of the on-crest phases. To test this, we repurposed a single BPM arrival time phasing procedure typically used to phase the injector buncher cavity and last two ICM SRF cavities. This method measures the arrival time at the downstream BPM while scanning the cavity phase by $\pm 60^{\circ}$ in small steps from its starting set-point and finding the minimum phase change, as this occurs when the beam accelerates on-crest. Unfortunately, this method runs into practical limitations for initial energies well above 6 MeV. Fig. 2.2.2 illustrates this point by plotting the phase change at $\phi_b = \pm 60^{\circ}$ as a function of voltage for each MLC cavity. For each cavity in the MLC, all upstream cavities are set to their nominal 6 MV voltage, and any downstream cavities are off. The dashed line indicates the typical noise level of the BPM phase reading (roughly 0.3°). These results predict the failure of this approach for all but the first two MLC cavities.

Beam based measurements of the on-crest phase via this method confirm this prediction. Fig. 2.2.3a and 2.2.3b show the results of this procedure when phasing the first cavity with an incoming beam energy of 6 MeV, and the second cavity with an incoming beam energy of 12 MeV. Note that use of the cavity hardware phase in these plots. The location of the BPM phase minimum corresponds to the cavity hardware phase for on-crest acceleration ($\phi_b = 0^{\circ}$). We estimate the resulting on-crest phase uncertainties to be roughly $\pm 0.8^{\circ}$ and $\pm 2.5^{\circ}$ for the two cases, respectively. Data taken for the remaining cavities show worse signal to noise, and we conclude that this procedure only meets the desired phase requirements of $\phi_{\text{error}} < 1^{\circ}$ when used to phase the first MLC cavity.

Due to the time constraints for the FAT, we decided on the following procedure to phase the remaining MLC cavities. Before turning on the cavity, the beam is steered to the first splitter viewscreen, IS1SCR01, and the position on that screen and the BPM before it recorded. Turning on the cavity and adjusting the phase until the beam returns to that same location on the screen determines one of the cavity zero-crossings. In the relativistic limit, the on-crest phase is roughly $\pm 90^{\circ}$ from this value, with the sign chosen to ensure the resulting phase increases the energy. During the FAT, operators performed this procedure by hand during tune up and the method thus currently lacks a systematic procedure for error estimates. Future continued use of this procedure requires both automation of the measurements involved, as well as systematic characterization of the accuracy of the resulting on-crest phase. Additionally, the potential use of a spectrometer set-up should also be investigated.

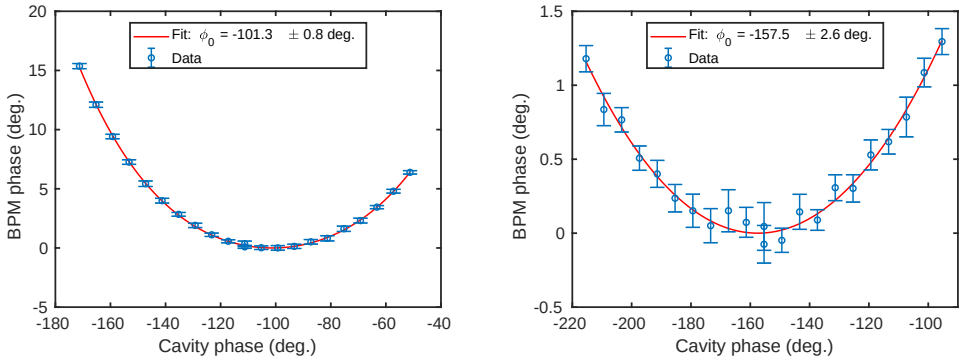

(a) First MLC cavity phasing with initial energy at 6 MeV.

(b) Second MLC cavity phasing with initial energy at 12 MeV.

Figure 2.2.3: Dependence of the arrival phase at BPM ID1BPC01 on the hardware phase of the first (a) and second (b) MLC cavity. The lower initial beam energy going into the first cavity results in larger BPM phase changes, and thus provides sufficient accuracy for the on-crest phase determination.

2.2.2 Main Linac Vertical Offset

Initial attempts at steering the beam through the center of the main linac cavities indicated an offset of the MLC with respect the BPMs on either side of the linac (IB1BPC03 and ID1BPC01). In particular, manual alignment of the beam in the first cavity suggested a vertical offset of roughly 5 mm. Consequently, more detailed measurements were performed to better quantify these observations. These measurements proceeded as follows: each cavity was turned on individually, with all other cavities turned off. In each transverse direction a pair of corrector magnets was used scan the beam's transverse position on the BPM just upstream of the MLC while keeping the corresponding beam's angle constant. For each incoming beam position in this scan, the phase of the cavity was then scanned from 0^o to 360^o in steps of 30^o, and the transverse positions on the downstream BPM (ID1BPC10) measured (sampled 5 times). We attribute any phase dependent difference in the beam position on the BPM downstream to off-axis cavity focusing. More specifically, for a specific input beam offset, the variance of the final beam positions over all phases provides a rough estimate of the beam offset relative to the cavity. Using this as our initial guide, we first performed scans in the horizontal direction in order to minimize any horizontal beam offset going into each cavity. The scanning procedure was then repeated for the vertical direction for each cavity.

Fig. 2.2.4a shows the vertical position on the downstream BPM as a function of the vertical upstream BPM position for the various values of the first cavity (RD1CAV06) phase and a cavity voltage of 500 kV (all other cavities were measured at 1000 kV). For a given cavity, the data clearly imply a linear relationship between BPM readings. The linear relationship in the data suggest analysis of the problem using linear beam transport. Assuming no x-y coupling, the vertical position y_f on the downstream BPM takes the form

$$y_f(\phi) = m_{33}(\phi)y_i + m_{34}(\phi)y_i' + (1 - m_{33})y_{\text{cav}}. \tag{2.2.3}$$

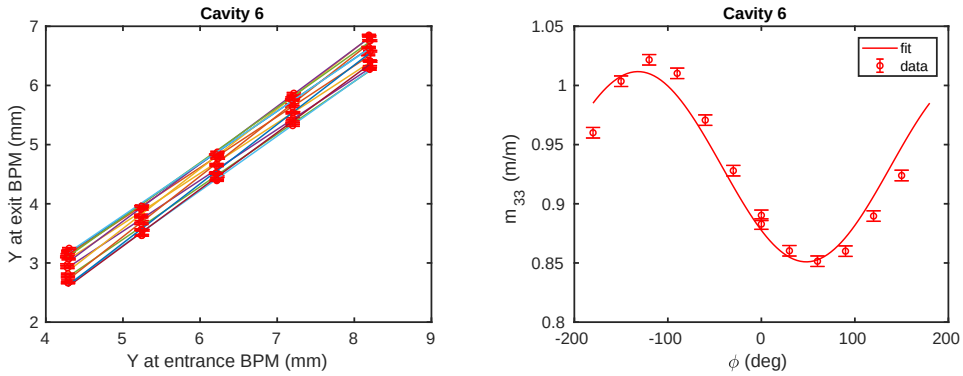

(a) Example BPM data taken for the first MLC cavity.

(b) Resulting measured BPM slopes for the first MLC cavity.

Figure 2.2.4: Example vertical position and phase scan data for the first main linac cavity: (a) shows the linear relationship of the incoming beam position to the beam position after the cavity for various cavity phase settings, while (b) shows the phase dependence of the slopes in (a) and the resulting fit using Eq. (2.2.4).

where m_{33} and m_{34} are elements of the transfer matrix $m_{i\to f}$ from the upstream to downstream BPM, ϕ is the cavity phase, and $y_{\rm cav}$ is the vertical offset of the cavity. In this expression the initial beam position at the upstream BPM $y_i = y_i(I)$ depends on the current I in the paired correctors. Linear fitting to the data in Fig. 2.2.4a directly determines the phase dependent slope term m_{33} in Eq. (2.2.3). To determine the cavity offset, we assume the angular term is small, and fit both the m_{33} and residual offset term $(1 - m_{33})y_{\rm cav}$ globally to two sinusoidal functions with a common phase offset:

$$\begin{aligned} m_{33} &= A\cos(\phi + \phi_0) + B, \\ (1 - m_{33})y_{\rm cav} &= C\cos(\phi + \phi_0) + D. \end{aligned} \tag{2.2.4}$$

Here A, B, C, D, and ϕ_0 are the fit parameters. Fig. 2.2.4b shows the resulting sinusoidal best fit for the slope $m_{33}(\phi)$. Equating the cosine terms in these equations results in an expression for the cavity offset: $y_{\rm cav} = -C/A$. Repeating this procedure for the data for each cavity results in the estimated cavity offsets shown in blue in Fig. 2.2.5. Also shown (in orange) are the initial cavity offset estimates based on minimizing the spread of phase dependent vertical downstream BPM positions for each incoming beam position. Note the agreement between the two methods. These measurements result in an average cavity offset of roughly 5.5 mm. To justify these results further, we computed the m_{33} and m_{34} transfer matrix elements from upstream to downstream BPM with using field maps of the MLC cavities scaled to corresponding cavity voltages used in the offset measurements. From these results, we judge that the analysis presented above requires the angle term $y_i' < 1$ mrad. We estimate the angle to be somewhere on the order of $0.1 - 1$ mrad, justifying this method. As a consequence, further surveying of the beamline, BPMs, and MLC are planned, and pending the results of these measurements, movement of the linac cryomodule may be called for.

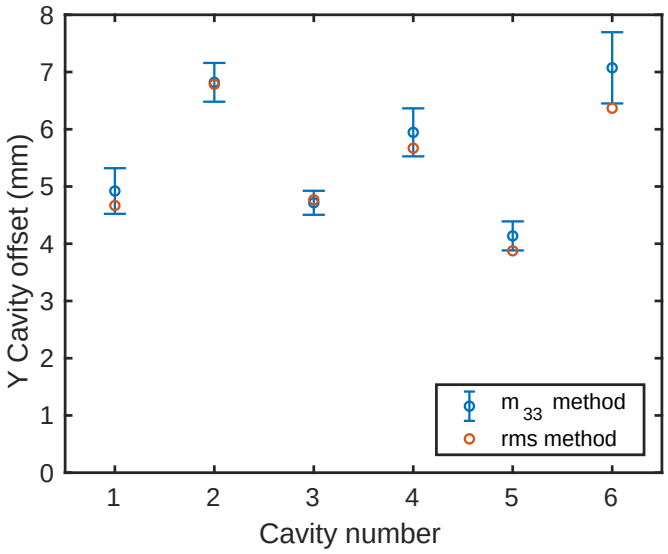

Figure 2.2.5: Vertical MLC Cavity offsets.

2.3 S1 Splitter Line Commissioning

2.3.1 Splitter Line BPM Nonlinearity Correction

In general, the particular method used to convert the BPM button signals into beam positions fundamentally limits the accuracy of BPM position data. While computationally simple, the well known "difference over sum" method for four button signals typically introduces large errors for beams significantly off axis. As a consequence, many methods exist to correct this effect [6]. In the past, the CBETA/Cornell injector stripline BPMs made use of an analytic expression for the four BPM signals. This approach approximates the BPM signals as proportional to the integral of the induced surface charge on the stripline due to an infinitely long circular conducting cylinder. The striplines are approximated as short arcs of the circular pipe, described only by the angle they subtend, θ_b [1]. The resulting expression depends only on the beam position (x, y), pipe radius R, and θ_b. Inversion of this expression for the beam position (x, y) is achieved using a χ^2 fit of the model to the real BPM signals. A similar procedure allows for correcting the BPM intensity. Note that as striplines are not actually 2D objects, we allow θ_b to vary in order to best correct the measured nonlinearity. This procedure results in corrected BPM positions over nearly the entire enclosed beam pipe area.

Since the publication of [1], modifications to the fitting process described have been made. In particular, the original routine fits for all four individual BPM signals, along with an overall scale. While this fitting method has the benefit of easily extending to arbitrary numbers and locations of BPM buttons, it results in increased sensitivity to scale errors between the associated signal pairs (top-bottom, left-right) in the 4 BPM signal case. Dividing out the

overall amplitude of each associated signal pair removes this sensitivity:

$$S_x = \frac{S_{\text{right}} - S_{\text{left}}}{S_{\text{right}} + S_{\text{left}}}$$
$$S_y = \frac{S_{\text{top}} - S_{\text{bottom}}}{S_{\text{top}} + S_{\text{bottom}}}$$

The new fitting method calculates these quantities and fits them to the measured values.

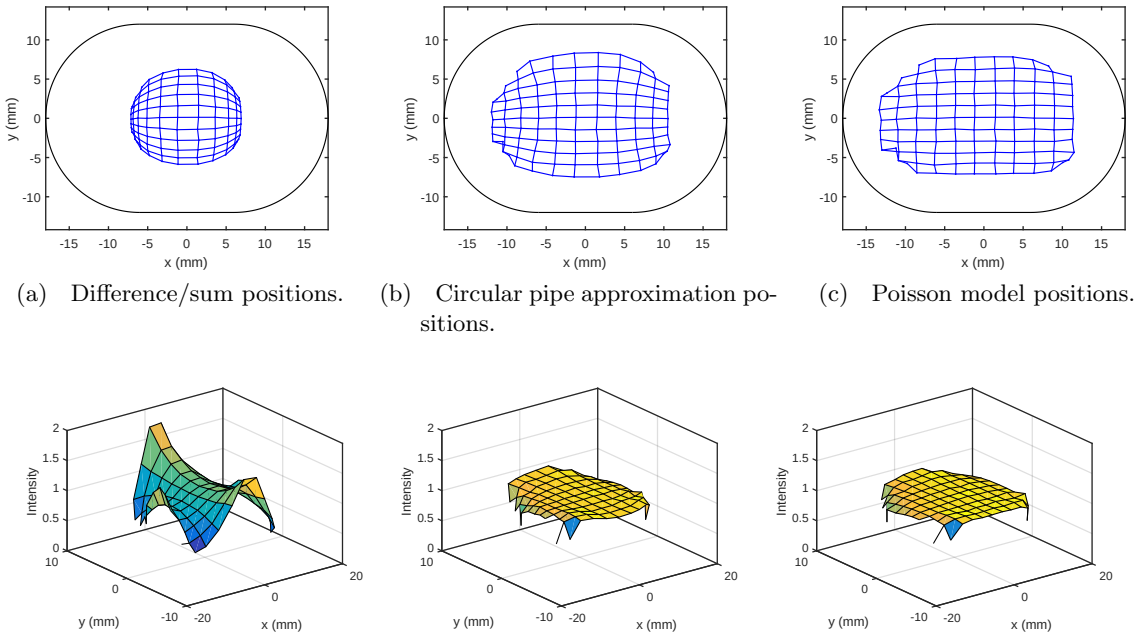

(a) Difference/sum positions. (b) Circular pipe approximation positions. (c) Poisson model positions.

(d) Difference/sum intensities. (e) Ccircular pipe approximation intensities. (f) Poisson model intensities.

Figure 2.3.1: Comparison of the beam positions and intensity using three different models to interpret the raw data from the BPM. First, a simple difference/sum model is used (a,d). Next, a correction is made using an approximation for a circular pipe (b,e). And finally, the model using a fieldmap from a Poisson calculation of the correct 2D pipe geometry is used (c,f).

The vacuum chamber in the S1 splitter section features a racetrack profile (see Fig. 2.3.1a-2.3.1c), with width of 36 mm and height of 24 mm. This violates the assumption of cylindrical symmetry made in the analytic model described above, resulting in decreased range of validity of the resulting BPM positions determined by this method. While the racetrack geometry precludes analytic treatment, programs such as Poisson [7] allow one to find a numerical solution to the 2D electrostatic BPM problem featuring the correct beam pipe cross-section using the method described by Helms and Hoffstaeter [8]. The generation of a look up table of beam positions from BPM signals based on this numerical approach allows for simple method

to interpolate and invert (via χ^2 fitting) the BPM signals for the BPM positions. Unfortunately the schedule of the FAT test prohibited the integration of this method into the control system, and thus its online evaluation. Instead, it turns out that replacing the beam pipe radius R with the average of the two inner radii of the pipe $R_{\text{avg}} = \frac{1}{2}(23.0/2 + 35.5/2) = 14.625$ mm significantly extends the range of validity of the analytic BPM method to a fraction of the beam pipe area suitable for initial commissioning efforts.

We quantified the effects of these methods by performing a rectangular scan of the beam position on the first S1 BPM (IS1BPM01) using the first horizontal and vertical dipoles in the splitter line (MS1DPB01 and MS1CRV01) and recording the corresponding BPM button signals. The signal data was then inverted to find the predicted BPM positions for each of the three methods: the standard "difference/sum" model ($x = \frac{R}{2} \cdot S_x$, $y = \frac{R}{2} \cdot S_y$), the modified analytic approximation with average radius, and the model incorporating Poisson generated fieldmaps for the 2D racetrack pipe geometry. In the latter two cases, the effective size of the BPM buttons was allowed to change to best correct the nonlinearity. The beam energy for all of these measurements was 6 MeV.

Fig. 2.3.1 displays the resulting beam positions and intensities measured. The top row shows the predicted beam positions, while the bottom row shows a corrected intensity of the beam, which is proportional to the total bunch charge. The results make clear that the simplest model produces accurate beam positions only within a few millimeters of the center of the pipe, and results in a reported intensity that varies greatly over the scanned area. Interestingly, the modified analytic approximation more than doubles the useful region of the pipe, out to at least ±5 mm in x and y. The corrected intensity is nearly flat, and a much better measure of the bunch charge. Finally, using the Poisson look-up table, the final amount of nonlinear curvature is nearly fully corrected, and the BPM intensity slightly more flat. The remaining slight curvature near the edge of the measured grid indicates beam clipping, as also seen in the decreased intensity.

2.3.2 Path Length Adjustment

The establishment of single or multi-pass energy recovery requires precise control of the return phase(s) of the beam(s) at the MLC. To achieve this, the CBETA design makes use of two adjustable path length chicanes in for each beam energy. Each chicane features a pair of remotely controlled translation stages for online control of the path length. In particular, the low energy S1 splitter line path length adjustment system provides up to 9.6 mm (or 15° at the speed of light) total path length adjustment during beam operation. Synchronous movement of the two stages ensures minimal stress is placed on the bellows connecting the chicane vacuum chambers. In the S1 splitter line these two stages are located directly under S1 dipoles MS1DIP04 and MS1DIP05, as shown in Fig. 1.1.2. A change in translation stage position of Δl results in a path length change Δs experienced by the beam given by:

$$\Delta s = 2\,(1 - \cos\theta_{\text{bend}})\,\Delta l, \tag{2.3.1}$$

where $\theta_{\text{bend}} = 23.3^{\text{o}}$ is the bend angle of the inner splitter chicane.

In order to test path length adjustment, we temporarily rewired the BPMs in the splitter line, making IS1BPM05 capable of reporting both position and beam arrival phase. With all cavities in the MLC turned off, we then steered a 6 MeV electron beam through the splitter line

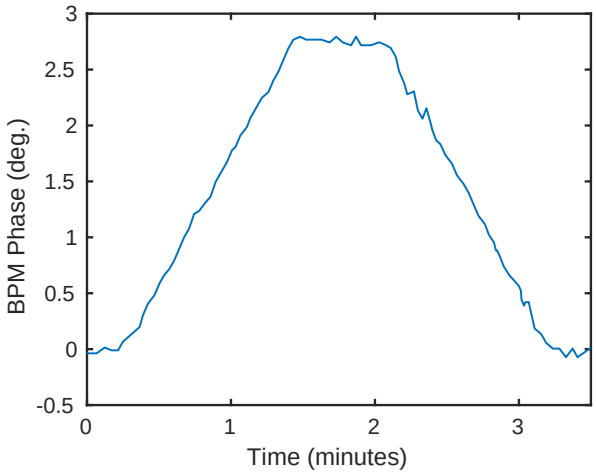

Figure 2.3.2: The beam arrival phase on S1 BPM 5 during a splitter stage movement forward and back of 1 cm.

and zeroed the reported BPM arrival phase. We then commanded the stage to move $\Delta l = +1$ cm and then back -1 cm, and recorded the measured BPM phase during the movement, as shown in Fig. 2.3.2. Eq. (2.3.1) implies a $\Delta l = 1$ cm stage movement results in a 1.63 mm path length change seen by the beam. This corresponds to a predicted BPM phase change of 2.54° [9]. The measured BPM phase data in Fig. 2.3.2 gives a measured BPM phase change of 2.8°, roughly 10% larger than expected. Translated into angle, this corresponds to a bend of $\theta_b = 24.5°$, or about 1 deg larger than the design value. One possible explanation for this discrepancy was that beam traveled through the chicane at a larger angle than anticipated from the zeroed orbit on the S1 BPMs. While more work is needed to understand and resolve this discrepancy, the measured path length change with beam demonstrate the ability to tune path length during operation, and thus constitutes a successful preliminary test of the proposed path length control in CBETA.

2.4 Measurements at 42 MeV

2.4.1 Dispersion and R_{56}

Dispersion η_x and R_{56} play important roles in controlling emittance dilution and establishing energy recovery in the full CBETA design, and thus necessitated experimental verification in the FAT. Scanning the voltage of the last MLC cavity allows for the simultaneous determination of both the dispersion η_x and R_{56} matrix element by measuring the orbit and arrival phase response on the downstream BPMs. Only the BPM directly after the linac (ID1BPC01) and first BPM in the FA arc (IFABPM01) were configured to read phase data for these measurements. Typical measurements scanned the voltage of the last MLC cavity in the range of ±200 kV around the desired set-point in 7 steps. At each scan point, the beam position and phase was measured 10 times at 5 Hz and averaged. The slope of resulting orbit and phase response as a function of voltage, along with the beam momentum, determine η_x and R_{56}.

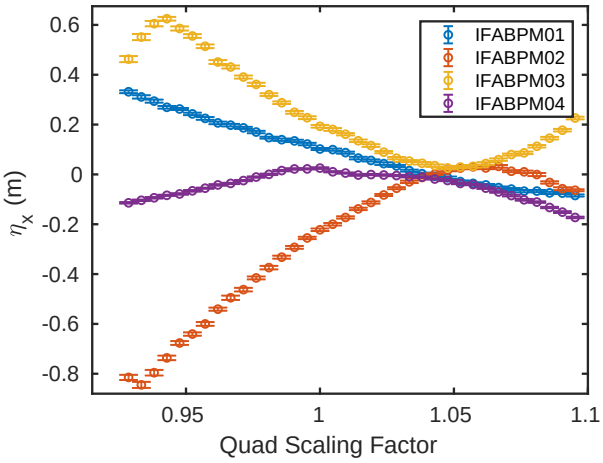

Figure 2.4.1: Dispersion measured in the FA section as a function of an overall scale of the S1 splitter quadrupoles. At around a factor of 1.04, the dispersion is minimized.

The splitter is designed to create a periodic dispersion in the FFA section. At the FA BPMs, that periodic value is −11 mm (see Fig. 1.1.3c). With the quadrupole currents at their design settings, we measured a non-periodic dispersion at the FA BPMs, with magnitudes as high as 0.4 m. To improve the dispersion, we first scaled all of the quadrupoles by the same scaling factor. Fig. 2.4.1 shows the measured dispersions as a function of the quadrupole scaling factor. The smallest magnitude of the dispersions occured when the quadrupole scaling factor was about 1.04, with a resulting dispersions having a maximum magnitude of about 0.1 m (still larger than anticipated). Starting from this scaling factor, we then attempted to use the model to further improve the dispersion, but we were unsuccessful. For all subsequent measurements, at all tested beam energies, this scale factor of 1.04 was applied to the splitter quads. Additional dispersion and R_{56} measurements were performed as a function of beam energy, and are discussed below in Sec. 2.5.2.

We note that the scaling factor applied to the splitter quads could arise from a number of sources: the energy could be incorrect; the quadrupole calibration factor could be off; or there could be some difference between the model and the actual machine. The fact that we never achieve a periodic dispersion with the expected value, and that an initial correction attempt failed when using the model indicates that a modeling error is contributing to the incorrect dispersion. To achieve the correct dispersion in the future, we will measure the response of the dispersion (and R_{56}) to quadrupole gradient changes and make corrections based on that.

2.4.2 Orbit Response

Measurement of the orbit response matrix provides a straightforward way of characterizing the single particle optics throughout the entire FAT layout, including verification of various magnet strength calibrations, and allows for comparison with the online simulation model. Additionally, use of the response matrix features prominently in various feedback routines

such orbit correction.

The procedure for measuring the orbit response on each BPM begins by scanning the corrector and dipole currents over a broad range (the full range in the case of correctors), and recording the beam position and intensity on all downstream BPMs. For each BPM, the data was truncated to include only those points within a small region around the BPM center, to best avoid BPM nonlinearity, and with intensity above a threshold, to avoid cases of lost or partially scraped beam. The slope of each line yields the corresponding orbit response in [mm/A].

Fig. 2.4.2 displays several example orbit response data sets, specifically, the first example of each type of dipole. The top row (Fig. 2.4.2a-2.4.2c) shows the response from correctors in the injector merger. The measured and simulated response on the BPMs upstream of the MLC show good agreement, however the two disagree once the beam passes through the linac. We point out that the BMAD lattice currently used in the online simulation makes use of a simple analytic cavity model instead of the realistic field maps for the cavities, and therefore may not accurately simulate the orbit through the MLC. Figs. 2.4.2d-2.4.2f show the BPM response to several S1 magnets downstream of the MLC. Here the measured data and simulated responses agree well, especially the horizontal orbit. For all of the simulations, the S1 splitter quad strengths were scaled in exactly the same manner as for the dispersion measurements discussed previously.

2.4.3 Grid Scan in the Fractional FFA Arc

Sending a grid of beam positions into the FFA arc and measuring the resulting positions on the FA BPMs provides a simple way of checking for BPM and magnet errors. Table-2.4.1 displays the scaling factors used to tie together the last horizontal dipoles and vertical correctors in the splitter line together. In the BMAD model of the machine, these pairs produce roughly 1 mm beam offsets with zero angle at the position of the first FA BPM. Fig. 2.4.3 shows the BPM positions when scanning the BPM offsets on the first FA BPM by ± 2 mm in nine steps. For each BPM, both the measured and corresponding simulated BPM data are shown, demonstrated reasonable qualitative agreement. The resulting data is fitting central data in each grid pattern on the k^{th} BPM to the following functions

$$\begin{aligned} x_k &= x_{0,k} + b_x x_1 + a_x x_1^2 \\ y_k &= y_{0,k} + b_y y_1 + a_y y_1^2 \end{aligned} \tag{2.4.1}$$

determines the derivatives $b_x = \partial x_k/\partial x_1(y=0)$ and $b_y = \partial y_k/\partial y_1(x=x_0)$ near the periodic orbit. For the case where the incoming beam angles with respect to the periodic orbit vanish: $x_1' = 0$, these derivatives represent the m_{11} and m_{33} transfer matrix elements from the first BPM to the downstream BPMs. Fig. 2.4.4b shows the comparison of the linear coefficients in Eqn. 2.4.1 to the predicted m_{11} and m_{33} matrix elements from the BMAD model of the FA section. Defining the horizontal and vertical relative error in the measured quantities as $(\partial x_k/\partial x_1 - m_{11})/\max(m_{11})$ and $(\partial y_k/\partial y_1 - m_{33})/\max(m_{33})$ implies the measured slopes agree with the theoretical matrix elements to within 7% for all three downstream BPMs. Here the use of the maximum in the transfer elements over the position range ensures the error doesn't diverge as the simulated quantities go through zero. Unfortunately, the position ranges in this scan did not allow for characterization of the FFA BPM non-linearity.

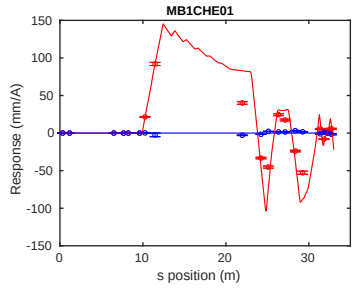

(a) First injector merger dipole trim.

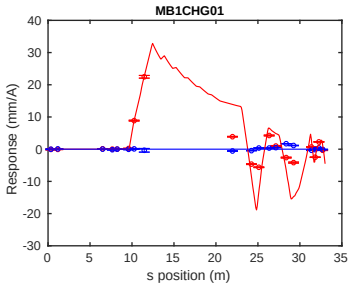

(b) First horizontal A3 corrector..

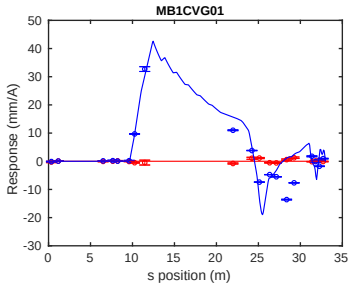

(c) First vertical A3 corrector.

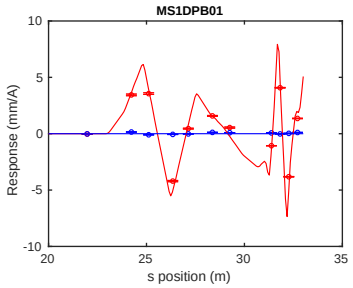

(d) First S1 splitter dipole, the temporary replacement for the common magnet.

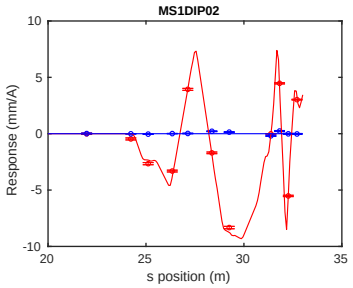

(e) Second S1 splitter dipole.

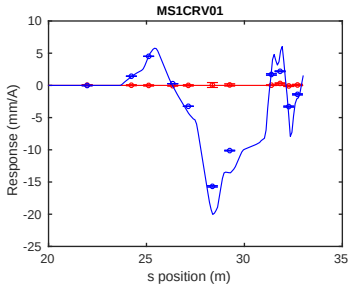

(f) First S1 splitter vertical corrector.

Figure 2.4.2: Measured orbit response to dipole magnet kicks (points) compared to prediction from simulation (lines). Horizontal response is shown in red, and vertical in blue. An example magnet is shown for each type of dipole encountered after the injector merger.

2.5 Measurements over a Broad Energy Range

The CBETA design features four accelerating passes through the linac, each with 36 MeV gain, requiring a factor of about 3.6 in energy acceptance through the FFA return loop. To study the machine behavior over as much of this energy range as possible, we transported a beam through the FFA arc at a number of energies, ranging from the the minimum energy required to form a stable periodic orbit through the fractional arc (roughly 38 MeV), to the maximum energy that the linac would let us reach (59 MeV). This allowed us to measure intrinsic properties of the FFA arc (betatron phase advance per cell and periodic orbit location), study our model of the splitter line by measuring dispersion and R_{56} near the end of the splitter line, estimate BPM offsets in the FFA arc, and determine a lower bound on the orbit distortions resulting from magnet errors in the FFA arc.

Performing the energy scan required computing new matched optics settings in splitter line at each energy set point. For each desired energy, we find the periodic orbit through the fractional FFA arc and the corresponding Courant-Snyder lattice functions ($\beta_{x,y}$, $\alpha_{x,y}$, η_x, and η'_x). Our goal is to find a set of dipole and quadrupole settings in the splitter line that

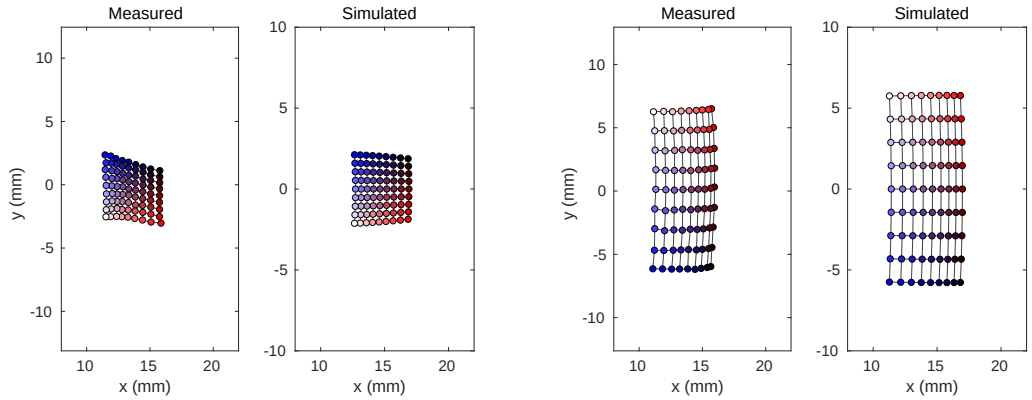

(a) Position scan measured on FA BPM 1.

(b) Position scan measured on FA BPM 2.

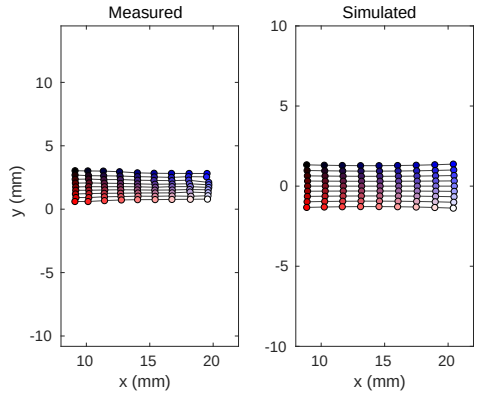

(c) Position scan measured on FA BPM 3.

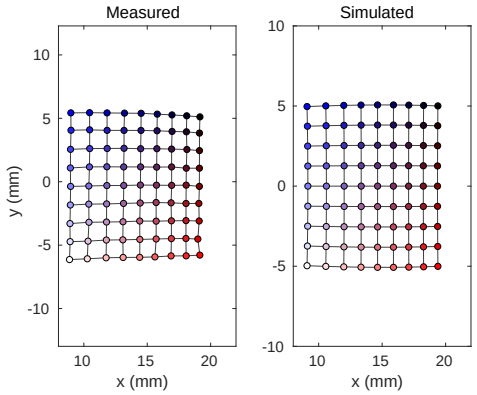

(d) Position scan measured on FA BPM 4.

Figure 2.4.3: FA BPM positions resulting from a single x, y grid scan going into the FA arc. For each BPM, the measured data is shown on the left, and the simulated data shown on the right.

match the beam coming from the linac to these values in the FFA arc. Furthermore, we will also require that the dipole and quadrupole settings make R_{56} from the end of the linac through the end of MS1DPB08 be about -15.3 cm. This is the value that, when our machine is configured for 42 MeV energy recovery, will give an R_{56} of zero for a full turn when both splitter lines and the FFA beamline are considered (and the other splitter line has the same R_{56} value).

To determine the quadrupole and dipole settings, we have an optimization process which starts from magnet settings at one energy and determines settings for a nearby energy. To do this we use a two-level nested optimizations. The inner layer has a fixed set of quadrupole gradients and begins with the dipoles set to their 42 MeV settings multiplied by the ratio of the beam momentum we are finding settings for to 42 MeV/c. It then adjusted the fields of MS1DIP06 and MS1DIP07 to steer the beam onto the periodic orbit in the FFA. For each evaluation performed in the outer layer, it chooses a set of quadrupole gradients, calls the inner

Table 2.4.1: Magnet combinations used for gird scan.

Horizontal Magnet	Unit Scale	Vertical Magnet	Unit Scale
MS1DIP07	-0.9303	MS1CRV03	0.1641
MS1DPB08	-4.0451	MS1CRV04	-1.2621

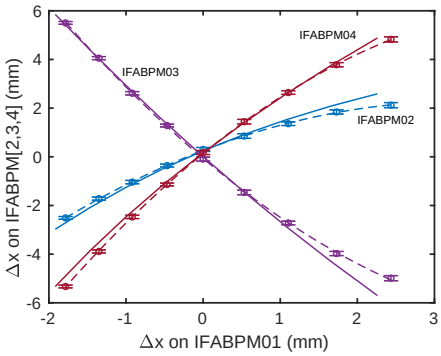

(a) Example of fitting for the m_{11} elements.

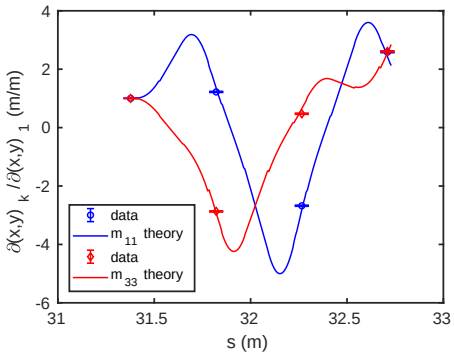

(b) Histogram of the vertical residuals.

Figure 2.4.4: Left (a): Fitting the position of of the downstream FA BPMs to the position on first FA BPM. The dashed lines show the resulting fit to the data, the solid lines indicate the prediction from the model. Right (b): The first derivative term for the x (blue) and y (red) data in (a). The solid lines show the m_{11} and m_{33} transfer matrix elements as a function of s through the FA line computed from the model.

Table 2.5.1: D1/S1 Splitter Magnet Current Settings (Amps)

Energy (MeV)	38	39	40	42	45	47	49	51	53	55	57	59
D1DIP01	1.55	1.59	1.63	1.71	1.84	1.92	2.00	2.08	2.16	2.24	2.33	2.41
S1DPB01	202.09	207.41	212.73	223.37	239.32	249.96	260.60	271.24	281.87	292.51	303.15	313.79
S1DIP02	57.33	58.84	60.35	63.37	67.90	70.92	73.93	76.95	79.97	82.99	86.01	89.02
S1DIP03	99.04	101.65	104.26	109.47	117.29	122.50	127.72	132.93	138.15	143.36	148.57	153.79
S1DIP04	73.98	75.92	77.87	81.76	87.60	91.50	95.39	99.29	103.18	107.07	110.97	114.86
S1DIP05	73.98	75.92	77.87	81.76	87.60	91.50	95.39	99.29	103.18	107.07	110.97	114.86
S1DIP06	99.49	102.11	104.61	109.47	116.63	121.34	126.02	130.66	135.28	139.86	144.42	148.94
S1DIP07	64.95	66.60	68.16	71.20	75.69	78.67	81.65	84.62	87.61	90.59	93.59	96.59
S1DPB08	190.05	195.05	200.05	210.06	225.06	235.07	245.07	255.08	265.08	275.08	285.09	295.09
S1QUA01	3.54	3.59	3.51	3.46	3.48	3.46	3.45	3.45	3.45	3.45	3.45	3.45
S1QUA02	7.65	7.58	7.46	7.47	7.60	7.58	7.54	7.49	7.43	7.36	7.28	7.20
S1QUA03	4.79	4.63	4.56	4.64	4.83	4.87	4.91	4.93	4.94	4.94	4.93	4.92
S1QUA04	10.44	10.13	9.90	9.96	10.28	10.36	10.42	10.47	10.50	10.51	10.51	10.50
S1QUA05	9.60	9.76	9.67	9.61	9.65	9.55	9.45	9.35	9.26	9.16	9.05	8.95
S1QUA06	0.30	1.06	1.49	1.82	2.11	2.23	2.34	2.43	2.50	2.57	2.63	2.68
S1QUA07	1.81	2.95	3.77	4.50	5.16	5.42	5.64	5.82	5.98	6.13	6.26	6.37
S1QUA08	3.96	3.28	2.57	1.92	1.46	1.24	1.07	0.93	0.81	0.69	0.58	0.48

layer solution process, then computes the Courant-Snyder lattice functions, and subtracts the target values computed as described in the previous paragraph. To find the optimal quadrupole gradients, the outer layer applies the equivalent of a nonlinear SVD optimization. One step of the optimization involves a computation of the Courant-Snyder functions, a computation of the derivative of those functions with respect to the quadrupole gradients, and finding a step in the quadrupole gradients that to linear order would match the Courant-Snyder functions while minimizing the sum of the squares of the quadrupole gradient steps.

To determine usable settings for the energy scan performed during the FAT, we first determined the lowest linearly stable energy in the model. This resulted in a lowest stable energy of 38.5 MeV. Starting with our settings for 42 MeV, we scaled the quadrupole gradients from their 42 MeV design values by the momentum ratio of 38.5/42, and found the settings for 38.5 MeV. We then stepped in 0.1 MeV steps up to our highest energy, using the quadrupole settings from the previous energy. Note that the settings that this process finds for 42 MeV will be different from the initial 42 MeV design values. Because we were able to find stable orbits in the machine for 38 MeV, (below the minimum 38.5 MeV in the model), we scaled the quadrupole and dipole settings by a factor of 38/38.5 to find the settings to use for 38 MeV.

Table-2.5.1 shows the results of this procedure for the energy settings eventually used in the following measurements. Note these values include a scaling factor of 1.04 for the quads, for reasons discussed previously (see Sec. **??**). Table-2.5.2 shows the MLC cavity set points for the corresponding energies. For each energy set-point, the appropriate settings from Table-2.5.1 were loaded into the machine. The dipoles were then adjusted slightly to zero the BPM positions through the splitter line and to steer the beam onto the periodic orbit in the FFA magnets.

2.5.1 Beam-based Magnet Calibration

The Fractional Arc Test presented the first opportunity to compare the S1-line magnet performance to the design specifications. Elytt Energy of Madrid, Spain [10] had produced and delivered six dipoles, eight quadrupoles and four vertical corrector magnets shortly before the final week of the test. Measurements from the six S1 BPMs and four FA BPMs were recorded for 6, 38, 42, 47 and 53 MeV beams, and again twice for the 42 MeV beam with the quadrupole magnets turns off, while scanning each of the magnets through eleven current settings. The

Table 2.5.2: MLC Cavity Voltage Settings (MV) used during Energy Scan (05/18/18)

Energy (MeV)	Cavity 6	Cavity 5	Cavity 4	Cavity 3	Cavity 2	Cavity 1	time
38	8.00	6.00	5.00	4.00	4.00	5.00	22:04
39	8.00	6.00	5.00	4.00	5.00	5.00	22:28
40	8.00	6.00	5.00	5.00	5.00	5.00	21:55
42	6.00	6.00	6.00	6.00	6.00	6.00	14:58
45	9.00	6.00	6.00	6.00	6.00	6.00	21:41
47	11.00	6.00	6.00	6.00	6.00	6.00	18:55
49	11.00	6.00	8.00	6.00	6.00	6.00	19:24
51	11.00	6.00	8.00	6.00	8.00	6.00	19:39
53	11.00	8.00	8.00	6.00	8.00	6.00	20.04
55	11.00	8.00	8.00	7.50	8.00	6.50	20:29
57	11.00	8.00	8.00	7.50	8.00	8.50	21:11
59	11.35	8.50	8.40	7.50	8.00	9.25	21:31

sixth setting was the nominal current setting. The dipoles were scanned over a range of ±10% of the nominal setting. The quadrupoles were scanned over a range extending from 0 A to twice their nominal setting. The vertical correctors were scanned over their full design range from -4 to +4 A. The work described in Ref. [11] analyzes a subset of the data, restricted to the measurements from the next BPM downstream of the scanned magnet. Figure 2.5.1 shows linear and cubic fit results for the horizontal beam position relative to the nominal trajectory at the S1 BPM 2, which is 0.629 m downstream of the end of the scanned dipole magnet S1DIP02. The cubic fit serves to account for the BPM nonlinearity described below in Sect. 2.3.1, since the measurements used here do not have the Poisson correction for the racetrack shape of the S1 beam pipe. The accuracy of the BPM measurements is exemplified in Fig. 2.5.2, which shows the measurements of the vertical beam position in S1 BPM 1 for each of the 11 current settings in ten downstream magnets in the case of the 42 MeV data set with quadrupole magnets turned off. The rms width of the Gaussian fit indicates a resolution of 0.038 mm, and a determination of the beam position of Y=4.333±0.004 mm. The comparable quantities for the horizontal beam position measurement are a resolution of 0.362 mm and a beam position of X=3.891±0.034 mm. These values include the effect of any jitter in the beam entering the S1 line.

The slope values in units of mm/A were used to determine the bend angle using the relative positions of the magnet center and the BPM. The transfer matrix elements between the dipole and the BPM were accounted for. Table 2.5.3 shows the results comparing the observed and expected values of the magnet strength calibration values in units of Tm/A. These results show the design strength of the dipoles to be confirmed with an accuracy of better than 1.5% for settings corresponding to beam energies ranging between 38 and 53 MeV, though the data set with quads turned off shows some as-yet-ununderstood anomaly. This study presents similar results for the strengths of the vertical corrector magnets, verifying the design values to an accuracy of about 1%. Slopes measured in the non-bend plane provided information on limits on roll angles, but again the accuracy was limited to tens of mrad by using only nearest-neighbor BPMs to reduce the correction for intermediate magnets, an accuracy exceeded by

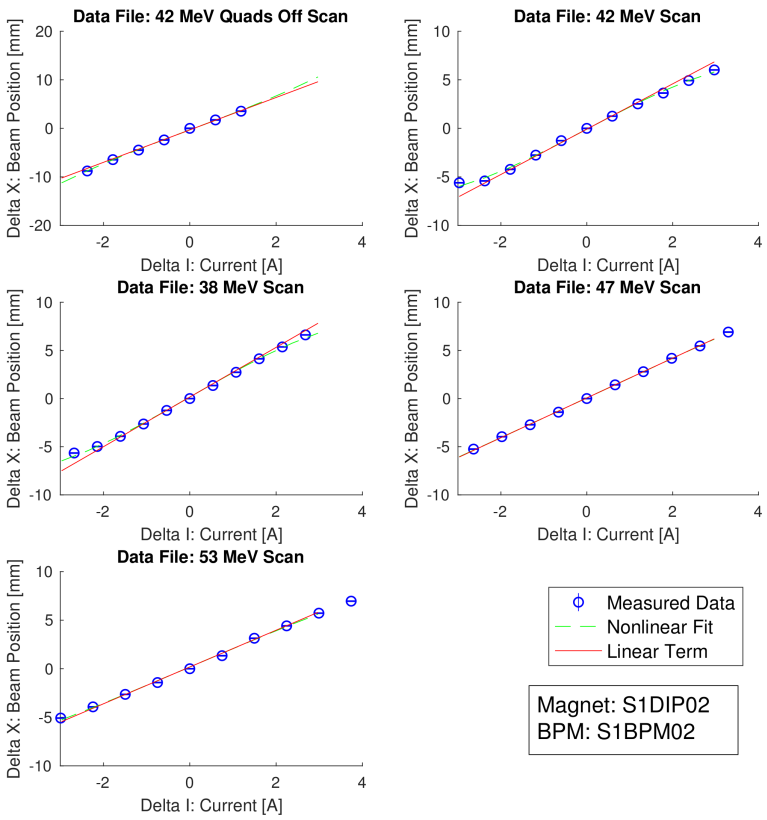

Figure 2.5.1: Results of fits to five data sets for the horizontal beam position at S1 BPM 2 as a function of the deviation of the S1DIP02 dipole magnet current setting from its nominal value.

	Bend angle (horizontal) at Nominal Current [Rad]	Horizontal Bend Angle / Current [Rad/Amp]	Calibration Value [Tm/A]	Expected Field Integral Along Trajectory [Tm/A]
42 MeV Quads Off	3.153e-01 ± 6.0e-03	5.31e-03 ± 1.0e-04	7.43e-04 ± 1.4e-05	6.98e-04
42 MeV Scan	2.975e-01 ± 4.7e-03	5.009e-03 ± 8.0e-05	7.01e-04 ± 1.1e-05	6.98e-04
38 MeV Scan	2.966e-01 ± 4.0e-03	5.535e-03 ± 7.4e-05	7.011e-04 ± 9.4e-06	6.98e-04
47 MeV Scan	2.922e-01 ± 1.9e-03	4.433e-03 ± 2.9e-05	6.946e-04 ± 4.5e-06	6.98e-04
53 MeV Scan	3.041e-01 ± 4.2e-03	4.067e-03 ± 5.6e-05	7.185e-04 ± 9.9e-06	6.98e-04

Table 2.5.3: Characterization Table of MS1DIP02 at IS1BPM02

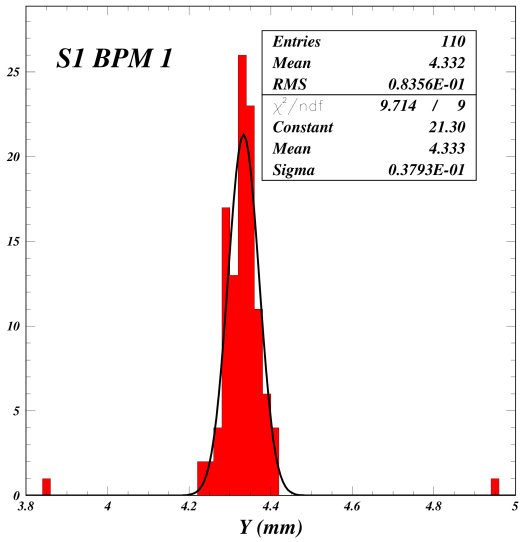

Figure 2.5.2: Reproducibility of the vertical beam position measurement at S1 BPM 01 for 110 measurements recorded during excitation scans of downstream magnets. The rms width of the Gaussian fit of 0.038 mm exhibits the accuracy of the measurement for the Y position of 4.333 mm.

the accuracy of the physical survey during installation.

A priority for future work is therefore to use the data from all the downstream BPMs for each magnet in estimates of its field strength as a function of current. The sensitivity will increase dramatically since the distance from magnet to BPM is increased from a few tens of centimeters to a few meters. Such analyses require the full lattice model including the machine state at the time of the measurements. A wealth of information on magnet calibrations, and magnet and BPM positions and angles can be expected to become available. The data also exhibits sensitivity to the scans of quadrupole strengths in a number of cases where the beam was not centered in the quadrupole and comparison of trajectories with the quadrupole turned off. This work will benefit from the newly available BPM measurement correction derived from the Poisson analysis described in Sect. 2.3.1, since much of the most sensitive measurements are derived from beam excursions of more than 5 mm from the nominal beam axis. Figure 2.5.3 shows the distance of corrected X,Y points from the uncorrected values over a range up to 2 mm from the beam pipe wall. The correction is numerically stable over this range, but the corrections range up to large values of more than 5 mm, so the analysis will have to include estimates of the range of validity of the correction and derivations of an uncertainty function.

2.5.2 Dispersion and R_{56}

At each tested energy, η_x and R_{56} were measured using the same procedure as mentioned in Sec. 2.4.1. Fig. 2.5.4a shows the raw data for an example dispersion data set taken by scanning the beam energy around the nominal 42 MeV beam energy using the last MLC cavity. The lines display a third order fit to the BPM data expanded around the nominal 42 MeV energy.

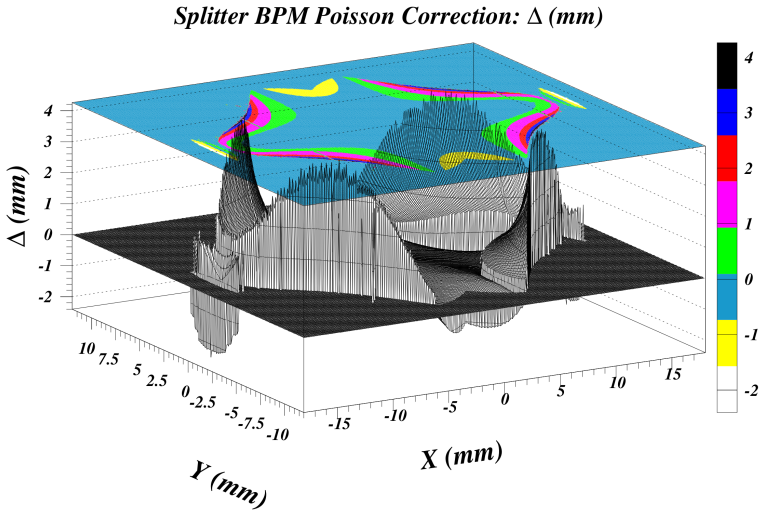

Figure 2.5.3: Illustration of the correction of BPM measurements for the racetrack shape of the vacuum chamber in the S1 line based on a Poisson electric field calculation. The vertical axis shows the separation between the corrected and uncorrected X,Y values, i.e. $\Delta = \sqrt{(X_{\rm cor} - X)^2 + (Y_{\rm cor} - Y)^2}$, set negative if the corrected point is closer to the center. The plot includes points up to 2 mm from the vacuum chamber wall. The separation values range from less than -2 mm to more than +4 mm.

Extraction of the linear coefficient yields the dispersion, defined here as $\eta_x = dx/d\delta$, where $\delta = (E\ [\text{MeV}] - 42)/42$. The resulting dispersion values are shown in Fig. 2.5.4b along with the

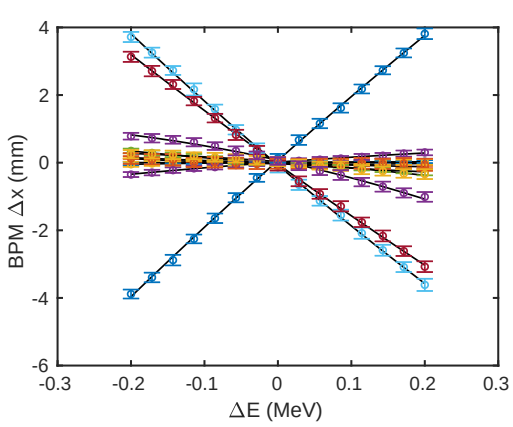

(a) BPM position change with beam energy.

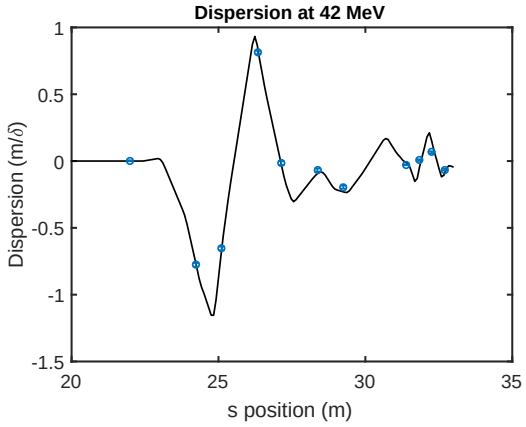

(b) Measured R_{56} and best fit model at 38 MeV.

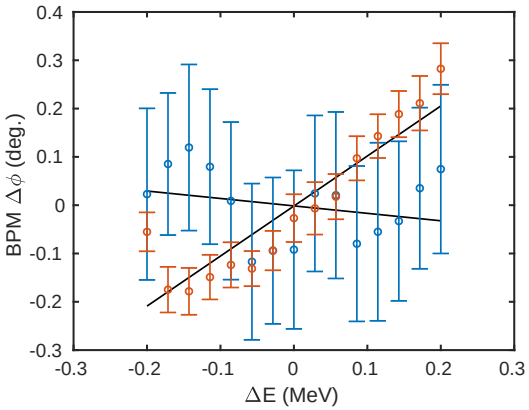

(c) BPM phase change with beam energy.

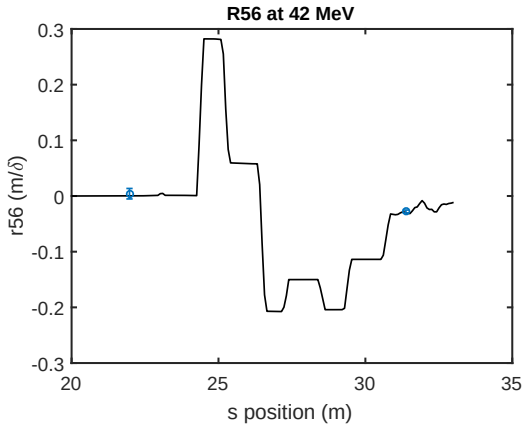

(d) Measured R_{56} and best fit model at 59 MeV.

Figure 2.5.4: Left: BPM position (a), and phase change (c) measured as a function of energy around the nominal 42 MeV energy. Right: the resulting dispersion (b) in the S1 and FA line and R_{56} in the S1 line (shown in blue) compared with the simulated values from the model (black line).

simulated prediction (shown in black). In addition to recording the BPM positions downstream of the linac during, the dispersion measurement procedure also saved the BPM phase on the first FA BPM in the fractional arc. The BPM phases corresponding to the disersion data in Figs. 2.5.4a and 2.5.4b is collected in Fig. 2.5.4c. A linear fit is applied to this data, which yields the R_{56} matrix element through the S1 section, defined here as $R_{56} = (c/\omega)d\phi/d\delta$, where ω is the angular frequency of the cavity and ϕ is the BPM phase change in [rad]. Fig. 2.5.4d displays the resulting measured R_{56}, as well as the coresponding simulated prediction from the CBETA-V online model. We point out that producing the excellent agreement between

simulartion and measurement seen in both the dispersion and R_{56} (Figs. 2.5.4b and 2.5.4d), required adjusting the the simulated S1 quadrupole settings by 1% in the model. Recall that this is in contrast to scale factor of 1.04 already used in setting the quadrupoles in the machine.

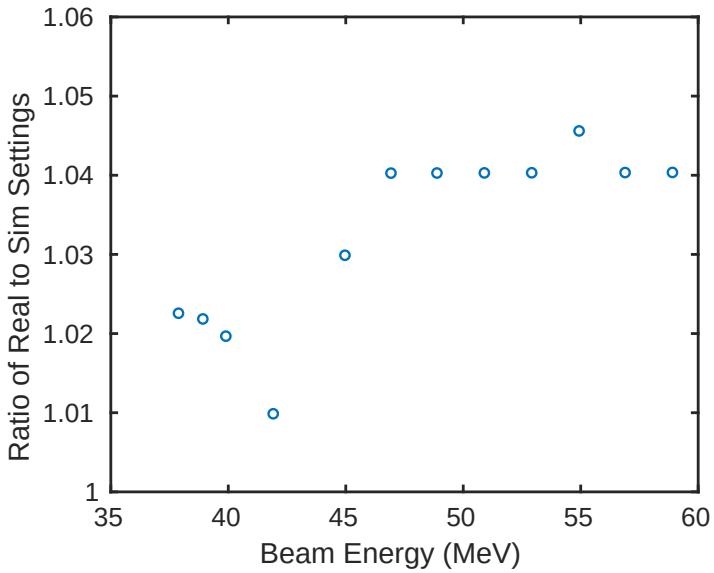

Figure 2.5.5: Ratio of the splitter quadrupole settings used during the measurement to the values used in the simulation. At each beam energy, this overall quadrupole scale was used to best fit the measured dispersion.

These measurements were repeated at each energy set-point and the simulated S1 quadrupole settings adjusted to bring the model η_x and R_{56} in agreement with the measurements. Interestingly, this scaling factor varied with energy. Fig. 2.5.5 shows the resulting best fit quad scales used to match the simulation to the measured values as a function of the beam energy. In this plot, a value of one indicates that the S1 quad calibration is the same in both measurement and simulation. Oddly, this most closely occurs for the 42 MeV, which contradicts the use of the original scale factor of 1.04 determined experimentally by minimizing the dispersion in the FA section at 42 MeV (see Sec. 2.4.1), and applied the S1 quad settings used in the energy scan. The values of roughly 1.04 shown in Fig. 2.5.5 for energies above 45 MeV indicate agreement with the original scaling factor determined in Fig. 2.4.1. Unfortunately, the schedule of the FAT precluded remeasurement of any of the data sets, and we can not draw a firm conclusion at this time as to whether the quad scale factor indeed changed for as yet unknown reason with energy or our assumption that it is due to a systematic error in quadrupole strength is incorrect.

2.5.3 Betatron Oscillations

Driving betatron oscillations at various amplitudes through the FFA arc and measuring the position response on the FFA bpms allows for determination of various lattice properties as a

Table 2.5.4: S1 Orthogonal Betatron Excitation Current Settings (Amps)

Energy (MeV)	38	39	40	42	45	47	49	51	53	55	57	59
S1DIP06:H1	-1.706	-1.766	-1.759	-1.709	-1.636	-1.594	-1.557	-1.525	-1.497	-1.473	-1.452	-1.434
S1DIP07:H1	-0.694	-0.834	-0.909	-0.922	-0.874	-0.833	-0.791	-0.750	-0.712	-0.676	-0.642	-0.610
S1DIP06:H2	0.224	0.319	0.442	0.601	0.761	0.844	0.916	0.982	1.043	1.101	1.157	1.212
S1DIP07:H2	0.167	0.230	0.317	0.426	0.526	0.572	0.608	0.638	0.662	0.683	0.702	0.717
S1CRV03:V1	-0.799	-0.763	-0.729	-0.708	-0.702	-0.703	-0.704	-0.705	-0.705	-0.706	-0.706	-0.706
S1CRV04:V1	1.398	1.296	1.178	1.074	1.008	0.983	0.963	0.945	0.927	0.908	0.888	0.866
S1CRV03:V2	0.781	0.761	0.750	0.758	0.778	0.791	0.802	0.812	0.820	0.827	0.833	0.837
S1CRV04:V2	-1.805	-1.752	-1.689	-1.653	-1.652	-1.661	-1.670	-1.680	-1.687	-1.693	-1.695	-1.695

function of energy. In particular, these include intrinsic properties of the FFA arc lattice cell, namely the periodic orbit position at the BPMs and the betatron phase advance per cell (i.e., the tune per cell). In addition, because the phase advance varies as a function of energy, we will be able to estimate the offsets of the BPMs in that arc. Finally, we will find parameters that provide a verification of our model for the splitter line.

At each of the energy setpoints specified in Tables 2.5.1 and 2.5.2, the beam was kicked using two linear combinations of the last two S1 splitter dipoles (MS1DIP[06,07]) and the last two vertical correctors (MS1CRV[03,04]). These linear combinations were chosen to correspond to a betatron oscillation with a maximum amplitude at the FFA BPMs of 1 mm. The two linear combinations were chosen to give betatron oscillations that were 90° apart in betatron phase. Each linear combination was multiplied by a factor which was scanned from -2 to 2 in unit steps. Only one setting vector was scanned at a time. For each setting, the beam position on the four FFA BPMs (IFABPM[01-04]) were recorded. This procedure was automated and tested with the online CBETA Virtual Machine before use. While taking the final measured data, the BPM readings were sampled 10 times at 5 Hz, and the average value and standard deviation saved for offline analysis. A single second pause was used between magnet setpoints to allow the beam to stabilize.

Our measurements at the m^{th} BPM and the n^{th} energy were fit in the least squares sense to the following functions:

$$\begin{aligned} x_{mn} &= \left(s \cdot A^{(1)}_{x,n} + B^{(1)}_{x,n}\right) \cos\left(2\pi m \cdot \nu_{x,n} + \phi^{(1)}_{x,n}\right) \\ &\quad + \left(s \cdot A^{(2)}_{x,n} + B^{(2)}_{x,n}\right) \cos\left(2\pi m \cdot \nu_{x,n} + \phi^{(2)}_{x,n}\right) + C_{x,m} + D_m \end{aligned} \tag{2.5.1}$$

$$\begin{aligned} y_{mn} &= \left(s \cdot A^{(1)}_{y,n} + B^{(1)}_{y,n}\right) \cos\left(2\pi m \cdot \nu_{y,n} \cdot + \phi^{(1)}_{y,n}\right) \\ &\quad + \left(s \cdot A^{(2)}_{y,n} + B^{(2)}_{y,n}\right) \cos\left(2\pi m \cdot \nu_{y,n} + \phi^{(2)}_{y,n}\right) + C_{y,m} \end{aligned} \tag{2.5.2}$$

$s^{(1,2)}_{x,y}$ are the scale factors of the kick, scanned from -2 to $+2$ in unit steps with only one of the four being nonzero. $A^{(1,2)}_{x,y,n}$ are the unit amplitudes of the two kicks used in each transverse plane at each energy; if our model is perfect they will be 1 mm. $B^{(1,2)}_{x,y,n}$ is the amplitude of the betatron oscillation with no additional kicks; if the orbit found by hand were the periodic orbit, these would be zero. $C_{x,y,m}$ are the (energy independent) BPM offsets. D_n is the (energy dependent) horizontal periodic orbit position; the vertical periodic orbit is known to be zero, so this term only appears in the horizontal function. $\phi^{(1,2)}_{x,y,n}$ are phase offsets of each betatron oscillation; $\phi^{(1)}_{x,y}$ and $\phi^{(2)}_{x,y}$ will differ by $\pi/2$ if out model is perfect. Finally $\nu_{x,y,n}$ are the tunes

per cell of the periodic orbit at energy E_n. The initial guess for $A^{(1,2)}_{x,y,n}$ coefficients was set to 1 mm. Similarly, the initial guesses for $B^{(1,2)}_{x,y,n}$, $\phi^{(1,2)}_{x,y,n}$, and, $C_{x,y,m}$ were set to zero, and the initial horizontal periodic orbit positions D_m guesses set to roughly 15 mm.

$\nu_{x,y}$ and D_n are intrinsic to the arc design; they give a measure of how accurate our model of the FFA arc is. $C_{x,y,m}$ give an estimate of the BPM offsets. Note that in the horizontal plane, there is a redundancy between $C_{x,m}$ and D_n; one can add a given constant to all of the $C_{x,m}$ and subtract that same constant from the D_n. We adopt the convention that the average of the $C_{x,m}$ is zero. For full turn energy recovery operation, in particular for 150 MeV energy recovery where we pass through the arc with four different energies, having an estimate of the BPM offsets will be extremely helpful for orbit correction since they will help distinguish between orbit offsets caused by magnet errors and position reading errors arising from BPM offsets. Thus a similar energy scan and fit will be performed for the full ring to obtain an estimate of the BPM offsets via this method. $A^{(1,2)}_{x,y,n}$ and $\phi^{(1,2)}_{x,y,n}$ give an estimate of the error in our model from MS1DIP06 through IFABPM01.

Fig. 2.5.6 shows an example of the fit to the horizontal (Fig. 2.5.6a) and vertical (Fig. 2.5.6b) BPM data at 42 MeV for both betatron oscillations, as well as the corresponding resulting fit residuals (Fig. 2.5.6c and 2.5.6d). For all horizontal/vertivcal positions we use an estimate of the error on the BPM positions of roughly 0.1 mm horizontally and 0.03 mm vertically, based on *all* of the BPM measurements taken during the energy scan. Fig. 2.5.7 collects a detailed analysis of the residuals. In particular, Figs. 2.5.7a and 2.5.7b display histograms of the horizontal and vertical residuals respectively. The corresponding variance of the horizontal and vertical residuals are 0.14 and 0.1 mm. Breaking down the residuals in Figs. 2.5.7a and 2.5.7b as a function of energy and BPM results in Figs. 2.5.7c and 2.5.7d, respectively. Note that average horizontal residuals vanish as a function of energy, and both the horizontal and vertical residuals vanish as a function of BPM index. This follows directly from the from the presence of the D_n term in the horizontal positions, as well as the $C_{x,y,m}$ terms in both the horizontal and vertical positions. These residuals give a lower bound of the orbit errors arising from magnet errors in the FFA. Those orbit errors could actually be larger since some of the actual orbit errors will lead to a shift of the fit parameters from their true values rather than a residual. When we have more cells in the arc, or if we had a larger energy range, the fit parameter would be more accurate and the residuals would be a better reflection of the true orbit errors.

The resulting fit parameters are displayed in Fig. 2.5.8. These include the resulting tunes as a function of the machine set-point energy (Fig. 2.5.8a), the energy independent BPM offsets (Fig. 2.5.8b, also in Table-2.5.5), the unit horizontal and vertical betatron amplitudes (Figs. 2.5.8c and 2.5.8d), the phase difference between the two betatron oscillations in each direction (Fig. 2.5.8e), and the measured and simulated horizontal periodic orbit positions as a function of energy (Fig. 2.5.8f). The error bars displayed correspond to the error in the fit parameters due to the above mentioned BPM position error estimates. In Fig. 2.5.8a the dashed lines show the corresponding prediction for the tunes, determined by tracking particles through 3D fieldmaps of the FA magnets and solving for the closed orbit, and displays good quantitative agreement.

Both the horizontal unit betatron amplitudes and phases shown Fig. 2.5.8c and Fig. 2.5.8e indicate an inaccuracy in the BMAD FAT model. In the former case the unit amplitudes were

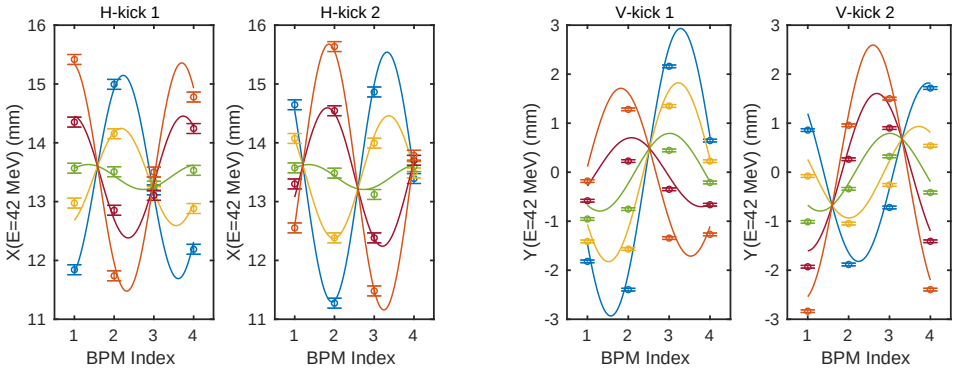

(a) Fit of model to horizontal 42 MeV data.

(b) Fit of model to vertical 42 MeV data.

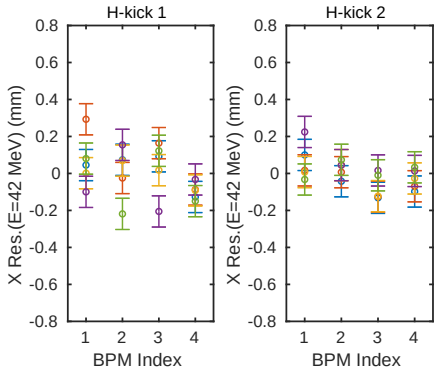

(c) Horizontal residuals at 42 MeV.

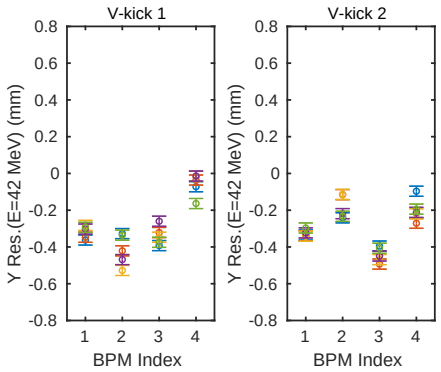

(d) Vertical residuals at 42 MeV.

Figure 2.5.6: Example data and model fits (top) and residuals (bottom) for the horizontal (left) and vertical (right) BPM positions on the FA BPMs for each value of the horizontal and vertical betatron oscillation kick(s) at 42 MeV.

designed to be 1 mm, in the later case the phase difference was intended to be 90 deg. In the vertical plane, the measured amplitude and phase difference is in good agreement with the model as can be seein in the vertical unit amplitudes in Fig. 2.5.8d and vertical phase shifts (red) in Fig. 2.5.8e. The horizontal periodic orbit position shown in Fig. 2.5.8f has an average systematic error with respect to the theoretical prediction for the orbit position of roughly 1.5 mm. This could arise from a nonzero average in the BPM offsets (though it is unlikely to be this large), non-linearity in the BPM response, a systematic difference between the modeled and as-built magnets, and possibly other effects. All of these measurements relied on the semi-analytic model discussed in Sec. **??** for the BPM nonlinear correction in FA BPMs. Unfortunately, direct measurement of the FA BPM non-linearity wasn't possible during the FAT, and this would lead to a systematic offset in the BPM readings at these amplitudes.

Upon comparing the tune data with the model in Fig. 2.5.8a, we sought to determine whether some of the difference could arise from energies being off by a uniform scaling factor (as a result of an energy calibration error, for instance). We therefore assumed that the

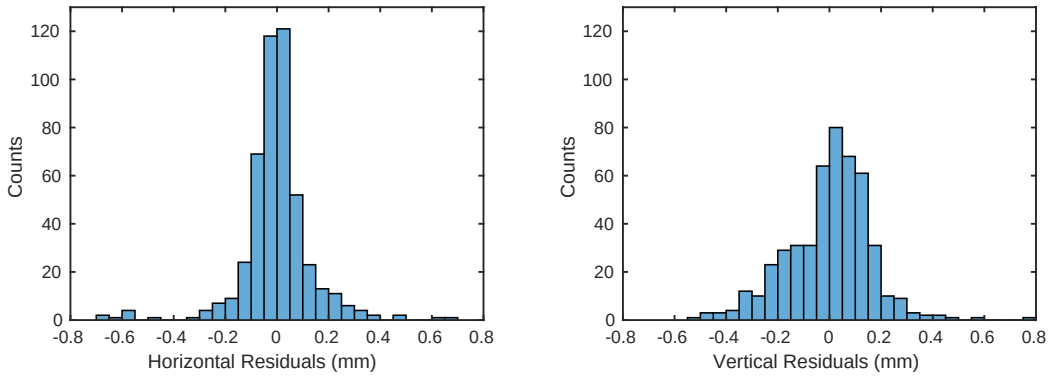

(a) Histogram of the horizontal residual

(b) Histogram of the vertical residuals.

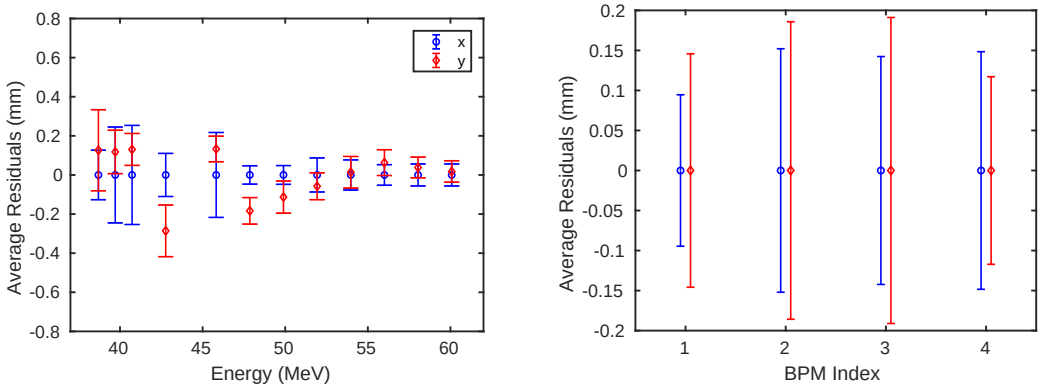

(c) Residuals vs. energy.

(d) Residuals vs. BPM index.

Figure 2.5.7: Top: histograms of the horizontal (a) and vertical (b) residuals. Bottom: the average residuals at each energy (c) and BPM (d).

Table 2.5.5: BPM offsets (mm)

BPM	X offset (C_x) (mm)	Y offset (C_y) (mm)
IFABPM01	-0.40 ± 0.02	0.70 ± 0.04
IFABPM02	-0.43 ± 0.02	0.34 ± 0.04
IFABPM03	0.28 ± 0.03	0.45 ± 0.04
IFABPM04	0.54 ± 0.02	-0.28 ± 0.04

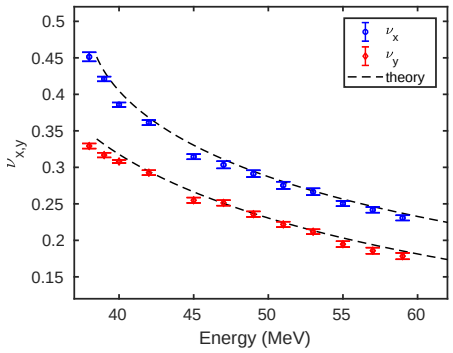

(a) Measured horizontal and vertical tunes.

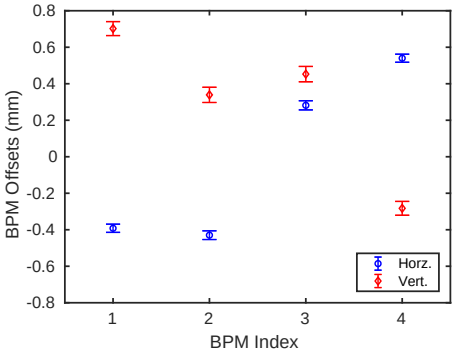

(b) Measured horizontal and vertical orbit offset.

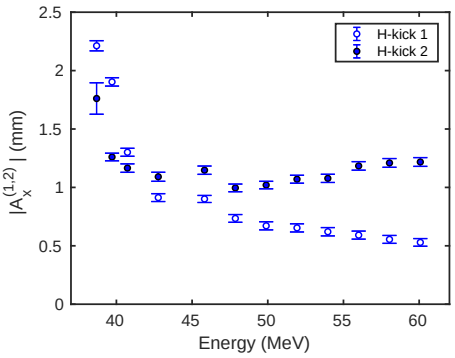

(c) Amplitude of horizontal orbit kicks.

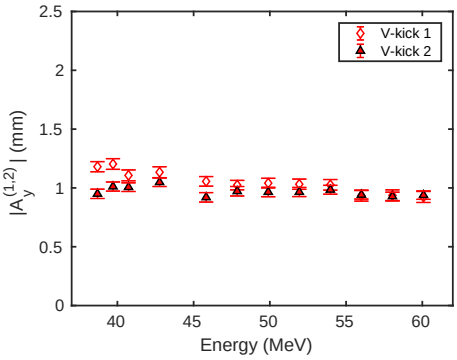

(d) Amplitude of vertical orbit kicks.

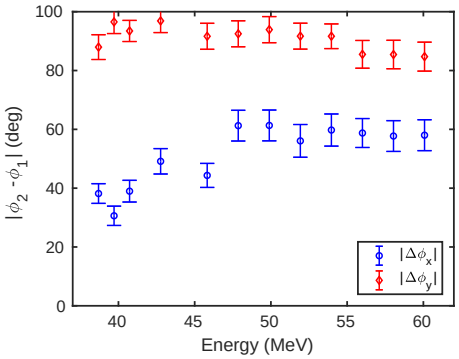

(e) Phase difference between pairs of horizontal and vertical kicks.

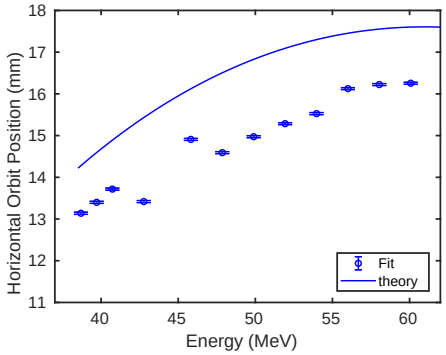

(f) Measured and simulated horizontal periodic orbit position.

Figure 2.5.8: Resulting fit parameters: tunes (a), BPM offsets (b), horizontal (c) and vertical (d) unit amplitudes, oscillation phase difference (e), and horizontal periodic orbit position (f). The solid line in (f) shows the simulated prediction for the periodic orbit position.

measured energies were scaled by the same factor for all energies, and performed a least squares fit of the measured tunes, multiplied by a scaling factor which the fit will solve for, to the theoretical tunes. Here we assume that the tunes depend on the energy E in the following manner: $\cos(2\pi\nu) = \sum_n b_n E^{-n}$. For simplicity we invert this relationship:

$$\frac{1}{E} = \sum_{n=1}^{6} a_{x,y}^{(n)} \cos^n\left(2\pi\nu_{x,y}\right). \tag{2.5.3}$$

and only keep the first six terms. This allows for a closed form solution for the best energy scale factor α (in the least-squares sense) of

$$\alpha \;=\; \frac{1}{2\langle E^2\rangle}\left[\left\langle \frac{E}{\sum_{n=1}^{6} a_x^{(n)}\cos^n(2\pi\nu_x)}\right\rangle + \left\langle \frac{E}{\sum_{n=1}^{6} a_y^{(n)}\cos^n(2\pi\nu_y)}\right\rangle\right].$$

This results in an energy scale of $\alpha = 1.018$. Note this puts the predicted tunes from 3D tracking nearly within all of the errorbars on the measured tune data, as seen in Fig. 2.5.9. Note that this scaling factor could arise not only from a systematic scaling of the energy, but also systematic error in the model of the quadruple magnets.

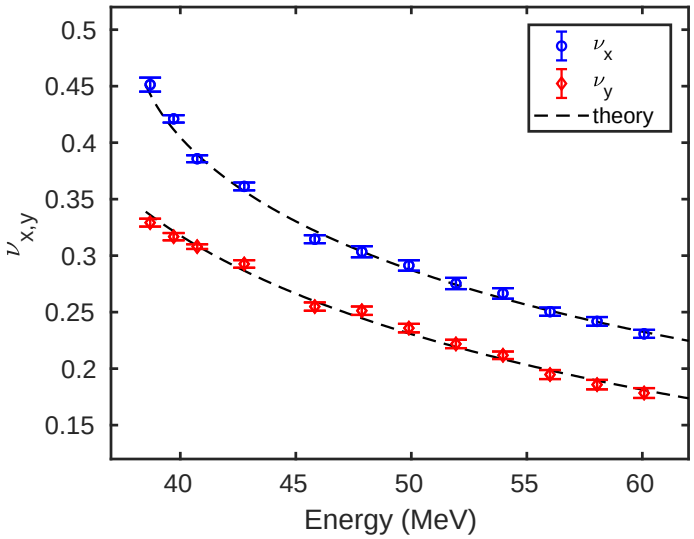

Figure 2.5.9: Measured horizontal and vertical tunes, compared to simulation, after best-fitting a systematic scaling of the energy.

Bibliography

[1] Gulliford, C., *et al. Demonstration of low emittance in the Cornell energy recovery linac injector prototype.* Phys. Rev. ST Accel. Beams, **16**, page 073401 (Jul 2013). doi:10.1103/PhysRevSTAB.16.073401.

[2] Gulliford, C., *et al. Demonstration of cathode emittance dominated high bunch charge beams in a DC gun-based photoinjector*. Applied Physics Letters, **106** (9), 094101 (2015). doi:http://dx.doi.org/10.1063/1.4913678.

[3] Bartnik, A., *et al. Operational experience with nanocoulomb bunch charges in the Cornell photoinjector*. Phys. Rev. ST Accel. Beams, **18**, page 083401 (Aug 2015). doi:10.1103/PhysRevSTAB.18.083401.

[4] Gulliford, C., A. Bartnik, and I. Bazarov. *Cold electron beams from cryo-cooled, alkali antimonide photocathodes*. http://arxiv.org/abs/1510.07738 (October 2015).

[5] Gulliford, C., *et al. Multiobjective optimization design of an rf gun based electron diffraction beam line*. Phys. Rev. Accel. Beams, **20**, page 033401 (Mar 2017). doi:10.1103/PhysRevAccelBeams.20.033401.

[6] Thieberger, P., *et al. Fast readout algorithm for cylindrical beam position monitors providing good accuracy for particle bunches with large offsets*. Review of Scientific Instruments, **89** (4), page 043303 (2018). doi:10.1063/1.5021607.

[7] http://laacg1.lanl.gov/laacg/services/download_sf.phtml (2012).

[8] Helms, R. W. and G. H. Hoffstaetter. *Orbit and optics improvement by evaluating the nonlinear beam position monitor response in the Cornell Electron Storage Ring*. Physical Review Accelerators and Beams, **8** (6), 062802 (June 2005). doi:10.1103/PhysRevSTAB.8.062802.

[9] Hoffstaetter, G. H., *et al. CBETA Design Report, Cornell-BNL ERL Test Accelerator*. ArXiv e-prints (June 2017).

[10] Elytt Energy, Orense 11, 28020 Madrid, Spain.

[11] E.Biddulph-West. *First Tests of Electron Beam Transport in the CBETA S1 Splitter Line*. CBETA machine note 028, Cornell University (2018).

3 Main Linac Commissioning

3.1 Introduction

The Cornell-BNL ERL Test Accelerator (CBETA)[18, 19, 26] project will be the first high-current multi-turn ERL employing Superconducting Radio Frequency (SRF) Linacs operating in CW. These are housed in two cryomodules, one for the injection system and the other used to execute energy recovery. The Fractional Arc Test (FAT) was an important funding milestone involving operations of both cryomodules at their design energy. The injector cryomodule[15, 17] consists of five 2-cell SRF cavities[21] and is configured to provide 6 MeV of energy gain to the electron beam for injection into the CBETA loop. It has been commissioned in multiple stages starting from 2009 and has reached a peak operating current of 70 mA in 2013[4]. The main linac[5, 7] on the other hand incorporates six 7-cell SRF cavities[10] with a design energy gain of 36 MeV and will be used to execute energy recovery. In this note, we detail our progress in commissioning the Main Linac Cryomodule (MLC) for the FAT.

Construction of the Main Linac Cryomodule was finished in Fall 2015[6, 9] with first tests in early 2016. Initial commissioning of the cryomodule included the first cool-down[8] during which various thermo-mechanical properties of the cryomodule were measured including precision alignment of the beam-line and the results were compared with model specifications. After the cryomodule reached 1.8 K, initial cavity testing in Self Excited Loop (SEL) was done to determine Q_L and Q_0 v/s E[12] followed by the first microphonics measurements[14]. The peak microphonics detuning was found to be much larger than the bandwidth for cavities which are not mechanically stiffened. These tests were followed by a warm-up for re-location of the cryomodule to it's final position for CBETA and a subsequent cool-down for further tests. The first major funding milestone was completed when we succeeded in passing beam through the MLC for the first time while operating a single cavity in May 2017[2, 11, 13]. The rest of 2017 was dedicated to testing all cavities individually for RF operations with special importance on finding the sources of vibrations and implementing an active compensation system for microphonics detuning. The most recent stage of commissioning was for the FAT where we operated the cryomodule with beam at it's design energy gain for the first time.

This note documents our progress in preparing the MLC for the Fractional Arc Test. The second section describes our test methods for the newly acquired solid-state RF amplifiers along with the passive components including the circulator describing results from our measurements and the issues we discovered. Then we describe our cryogenic system and discuss its operation. The next section details issues regarding cavity resonance including cavity tuning ranges, Lorentz Force and microphonics detuning. We describe the steps we took to reduce vibrations in the cryomodule and show results from our active compensation system. After this, we describe our RF commissioning procedure in detail and report our measurements on cavity field during beam operations for the FAT. Finally we summarize our key results and present a road-map to the future operations of the MLC with high current beam while executing energy

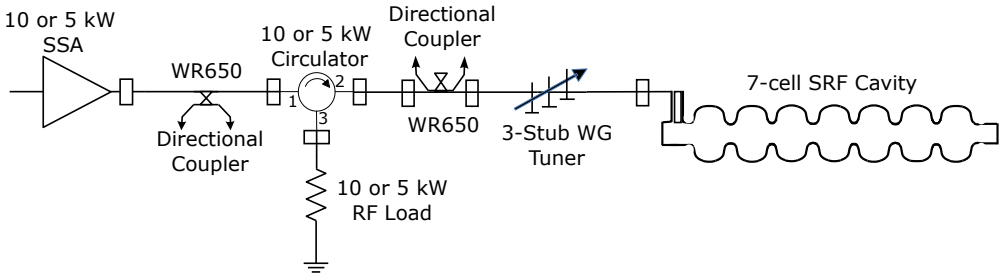

Figure 3.2.1: Typical RF power arrangement for one MLC cavity. We inserted a waveguide short between the fundamental power coupler of the 7-cell SRF cavity and the 3-stub waveguide tuner during tests of the Solid State Amplifiers (SSA).

recovery.

3.2 RF Systems

All six cavities of the MLC are powered by individual solid state amplifiers (SSA) connected to the cavity through a directional coupler, circulator and a 3-stub waveguide tuner as shown in Fig. 3.2.1. There are two sets of high power RF components capable of 5 kW and 10 kW for stiffened and un-stiffened cavities (Fig. 3.4.1) respectively. All these components were tested to full power before the FAT to understand their characteristics and verify operational readiness.

3.2.1 Solid State Amplifiers

Six SSAs were purchased from SigmaPhi Electronics, France, three with a maximum power capability of 5 kW and three with 10 kW. Some of their specifications are listed in Table 3.2.1. Both type of SSAs use the same enclosure, making it possible to upgrade the 5 kW units to 10 kW. Each enclosure contains one RF Driver module and, depending on SSA nominal output power requirement, several RF power modules. Maximum output power for a module is 2 kW. A 10 kW unit has six RF power modules, a 5 kW unit has three modules. Respectively, the maximum output power for the SSAs could be 12 kW and 6 kW. The SSAs were tested to 10 kW and 5 kW, and not tested to these maximum power levels.

Figure 3.2.2 shows an SSA cabinet with six installed modules. Each of water cooled 2 kW RF power modules is comprised of four RF pallets. An RF pallet is an electronic board with a 500 W 1300 MHz transistor, circulator, and load. The 2 kW modules are easily removed from the cabinet. A single control board can control up to two RF power modules. This combination of control board and power modules is sometimes referred to as an RF Slice. A 5 kW SSA would have 2 slices, a 10 kW SSA would have 3 slices.

The modular design of the SSA implies that it can continue to operate with multiple failed RF power transistor pallets. As a part of the RF base pallet, each transistor is protected by its own circulator. The power load on this circulator can withstand 500W. According to the manufacturer, when the SSA is operated with an external circulator, operation can continue

RF Power Input	~ 0 dBm (1 dB compression)
RF Power Output	5 kW / 10 kW CW @ 1300 MHz.
RF Stability	Amplitude: 0.1% rms,
	Phase: $< 0.1°$ rms
Bandwidth	1 MHz
Small Signal Delay	~ 100 ns
Phase Variation	$< 10°$ from 200 W to full power
Harmonic Power	-30 dBc at 10 % - 50 %
	and 100 % of 5 kW / 1300 MHz
Spurious Power	-70 dBc at 10 % - 50 %
	and 100 % of 5 kW / 1300 MHz
Noise	~ 8 dB
Cooling Water	30° C
	(Cornell is using 18° C water)
Efficiency	41 %
Input Voltage	400 VAC 3 phase
Nominal Gain	65 dB (measured)
Network Interface	TCP/MODBUS (RG45)

Table 3.2.1: Specifications for the solid state amplifiers from Sigmaphi.

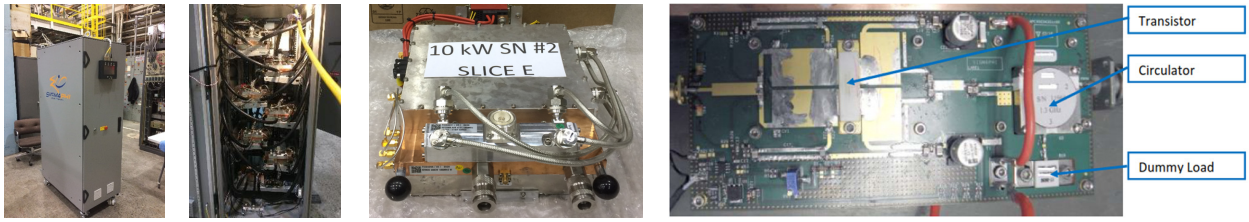

Figure 3.2.2: Images showing the SSA cabinet, the placement of the power modules, a single module and an internal pallet respectively.

even if there are one or more transistor failures with an net output power P_o given by,

$$P_o = P_t\left(\frac{N - N_f}{N}\right)^2 \tag{3.2.1}$$

Where P_t is total power without transistor failures, N and N_f are the total number and the number of failed transistors respectively. For example a 5 kW SSA having three RF power modules (at 2 kW power per module) can deliver 6 kW with all transistors operational. Output would be 5.125 kW if one transistor failed. Concerning the SSA reliability, the manufacturer has gained much experience since 2011. In the past four years (as of October 2016), 1800 transistors have been installed with 0.9 % suffering infant mortality.

MLC SSA system integration employs several layers of connectivity. A TCP/MODBUS interface and an Allen Bradley Control Logix PLC (Programmable Logic Controller). Both interfaces have a dedicated EPICS IOC allowing the similar levels of control and monitoring. The PLC was included as a precaution to ensure remote operation and appropriate interlock

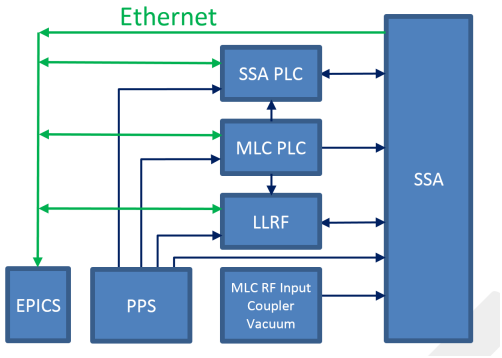

Figure 3.2.3: Simplified diagram of SSA control integration.

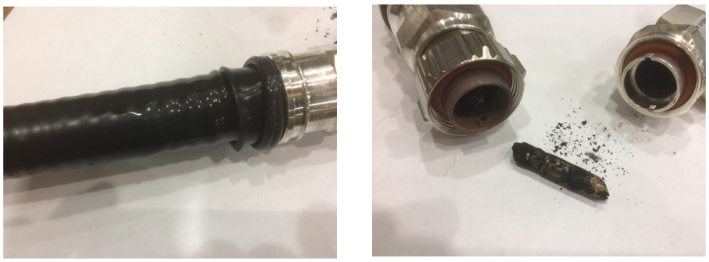

Figure 3.2.4: Damage to an internal cable connecting a single module to the power combiner in a 5 kW SSA which led to the failure of the associated power module.

redundancy in the event that the TCP/MODBUS interface did not work. SSAs also include a touch screen and push buttons on each unit for local control. Mounted on the touch screen is a key switch where LOCAL/REMOTE modes can be selected. The simplified diagram in Fig. 3.2.3 shows a portion SSA control integration.

There are several paths to control and monitor the SSA. Of particular importance are redundant paths for shutting down RF power. Personnel Protection System (PPS) has one direct path along with three other paths for shutting down RF Power. Equipment protection for the system is implemented through the two PLCs, (SSA and MLC), the LLRF, and a direct MLC cavity beamline vacuum signal. Interlocks external to the SSA include the Personnel Protection system (PPS) MLC vacuum and cryogenic control. The SSA has internal interlocks that protect the amplifier from excessive forward, reflected powers, high temperature, etc. An additional interlock was installed to monitor the reflected power on the SSA output waveguide (upstream of the circulator as shown in Fig. 3.2.1). The LLRF system is set to shut down the drive if reflected power is above 50 W. While the SSA has a reflected power interlock and can tolerate 30 % of forward power getting past the circulator, it is preferred to have a reflected power interlock independent of the SSA. This scheme provides an early warning that the circulator may not be working well.

The SSAs were evaluated individually starting with a simple AC power on test (no RF drive) to verify all controls were functioning. The interface with the PLC was successful in all SSAs though the MODBUS interface with one of the 5 kW modules failed. Next for the

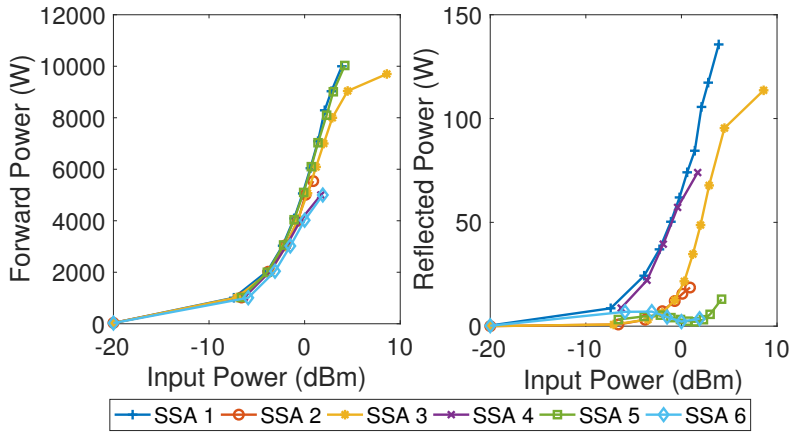

Figure 3.2.5: Transfer function measurement of the 6 Solid State Amplifiers (SSA) used for the 7-cell cavities. While odd numbered SSAs powering un-stiffened cavities are capable of reaching a forward power of 10 kW, the even numbered ones power the stiffened cavities with a maximum forward power of 5 kW. Left panel shows the forward power as a function of input power, while the right panel shows the power reflected into the SSA from the circulators.

RF power test, a drive signal from a standalone generator was applied and forward power was measured in 1 kW increments using the internal SSA directional couplers connected to external power meters. Waveguide was shorted just upstream of the input coupler providing a full power reflection back to the circulator which was measured in the same way. A damaged internal RF cable (Fig. 3.2.4) led to the failure of a single RF power module on a 5 kW SSA. The initial power tests also exposed problems with the circulators as we explain in the next section. Figure 3.2.5 shows the final measurements after necessary repairs indicating satisfactory performance of all SSAs.

3.2.2 Circulators

Each type of SSA (5 kW and 10 kW) requires a power circulator for protection from a full reflection of when there is no load on the SSA and their arrangement is shown in Fig. 3.2.1. The two conditions of no load are a shorted waveguide for calibration and testing and a cavity with no beam loading. Typical RF power circulators are three port devices. Power goes into port 1 and out of port 2. Reflected power comes back to port 2 and directed to port 3 which is connected to an external matched load. The circulators installed on the MLC SSAs shown in Fig. 3.2.6 appear to be two port devices but are actually three port. These circulators use an integrated water-cooled ferrite load that forms an inner conductor installed in the tapered waveguide. It is fitted with two 1 inch aluminum screws for isolation adjustment/tuning. The screws have a plastic piece on the internal end that prevent electrical shorting between the tapered waveguide and the ferrite load. The performance parameters are listed in Table 3.2.2.

During the initial SSA testing circulator tuning screw temperature was high, some of the screws reached $90° C$. For each SSA test, the circulator was fitted with a PMT arc detector.

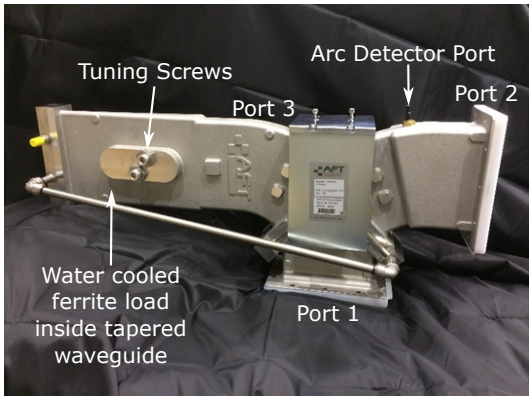

Figure 3.2.6: RF circulator from AFT used for the MLC RF system.

Waveguide	WR650
Center Frequency	1300 MHz
Bandwidth	10 MHz
Isolation	~ 26 dB @ 1300 MHz
Insertion Loss	< 0.2 dB @ 1300 MHz
Cooling Water Temp	Range: 25° C to 35° C
	Optimal: 30° C
	Cornell is using 85° F water
Water Flow	900 l/hr (10 kW),
	600 l/hr (5 kW)
Relative Humidity	80 % max
	(no condensation allowed)

Table 3.2.2: Specifications for the circulators from AFT.

The arc detector was checked for proper operation prior to SSA testing. No light was detected throughout the entire SSA testing and operating period, it is not clear why. The arc detector port points down and away from the ferrite load and circulating ferrites (Fig. 3.2.6). In addition the aperture is small and made for a fiber optic, it may be the case that the chosen mounting scheme for the PMT was not adequate. It should be noted that the power levels for this system is low and arcing is not expected. A visual inspection of the internal surfaces of the circulator showed severe burning of the plastic on the screws. In several circulators the plastic was vaporized and condensed on the circulating ferrites(Fig. 3.2.7). After consulting with AFT, it was discovered that the plastic piece installed on the end of the tuning screws had a much higher loss tangent than intended. An operational deadline existed and the window for repair was narrow. MLC cavity operation required 20 % average SSA power to operate and get through the fractional arc test (FAT). An agreement was reached that RF operation could proceed and the FAT milestone was successfully achieved under these severe limitations.

Once the FAT milestone was achieved, AFT sent a field engineer to replace the damaged plastic and cleanup the circulators. When work began, the ferrite loads were removed and additional damage was discovered in the form of broken load ferrites and in some cases severe

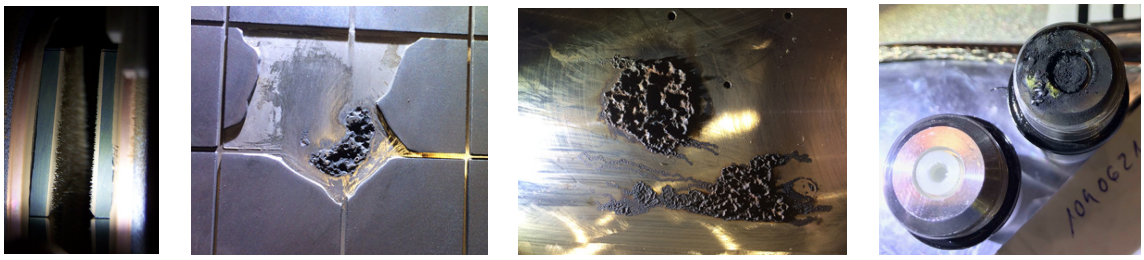

Figure 3.2.7: Images from damaged circulators. The panels show ferrites on a 5 kW circulator contaminated with plastic insulator material, damage to the load plates on a 10 kW and a 5 kW circulator respectively. The rightmost panel shows a damaged screw and its replacement.

pitting of the ferrite load substrate (Fig. 3.2.7). This damage was very likely caused by arcing between the screw tips and the ferrite load plate due to excessive heating of the plastic screw tip leading to vaporization and electrical breakdown. The ferrite loads were cleaned up by abrading the surfaces and removing broken ferrite pieces. The internal surfaces of the circulator were cleaned by blowing dry nitrogen and attempting to vacuum where possible. For two of the circulators, the ferrite load was installed with the broken ferrites facing away from the tuning screws because of the severe pitting of the substrate. Each circulator was tested at low power with a network analyzer and the isolation with this method was $\sim 26\,\mathrm{dB}$. Post repair high power testing revealed normal operating characteristics with screw temperatures never exceeding 39° C (Fig. 3.2.8) and reflected power below 150 W.

3.3 Cryogenic System

The cryogenic system of the main linac cryomodule is shown in figure 3.3.1.[16] Separate vessels house the six cavities and are supplied liquid Helium through chimneys by the 2K - 2 phase pipe. The pressure exerted by liquid Helium on the cavity walls influences the resonant frequency of the cavities and needs to be regulated. Slow trends in this pressure give rise to very low frequency microphonics detuning ($\lesssim$ 1Hz) and tight pressure regulation requires the interplay of two control mechanisms. The Joule-Thomson (JT) maintains the liquid level in the 2K - 2 phase pipe and the external blower maintains the vapor pressure. Two separate proportional integral control loops actuate the JT valve and the pump to maintain the liquid level and vapor pressure in the 2K -2 phase at their set points respectively. During operations these also induce mechanical vibrations.

Cryogenic control is done with an Allen Bradley PLC. The PLC handles all control aspects of the system. Modifications to the control scheme were made to address cavity detuning due to microphonics. The 2K 2-Phase helium level control loop regulates liquid helium level (LHe) with fixed position JT (Joule Thomson), precool valves and resistive heaters. Both valves are pneumatically actuated; the differences between the two are in the flow characteristics or CV factor. With valves in a fixed position, the liquid helium level is regulated with a resistive heater. Heat load when RF power is on is enough to keep 2K 2-Phase heater from turning on. The 2K 2-Phase heater is not directly set up to level the cryogenic load. However, it

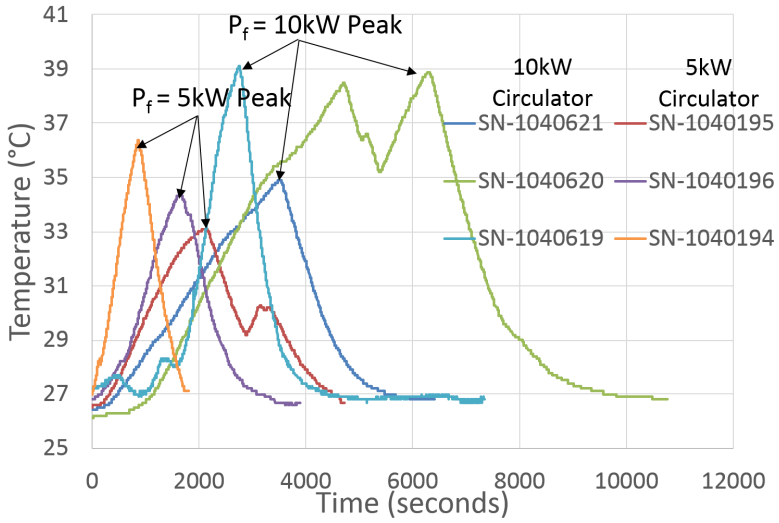

Figure 3.2.8: AFT circulator tuning screw temperature during high power test following tuning screw insulator replacement. Tests were not simultaneous and duration of tests varied for arbitrary reasons.

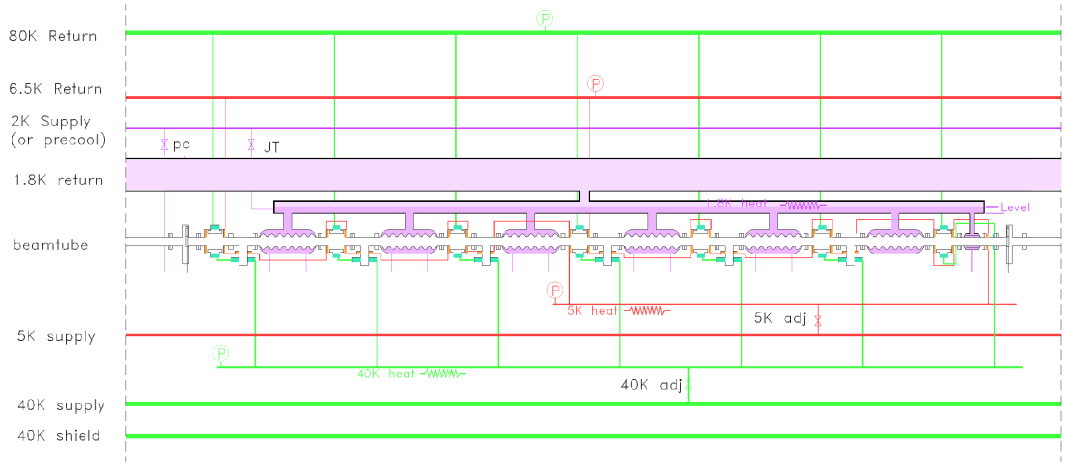

Figure 3.3.1: Schematic of the cryogenic system inside the Main Linac Cryomodule. Light and dark pink represent areas of gaseous and liquid Helium respectively. The 2 K liquid Helium supply line is connected to an external Heat Exchanger (HEx) can while the 1.8 K Helium Gas Return Pipe (HGRP) connects to external blowers which pump the boil off to maintain vapor pressure and hence temperature. The 2K - 2 phase pipe shown in the center of the diagram contains both liquid and gaseous Helium. The precool line connects to the bottom of the helium vessels and is used during warm-up and cool-down.

Pump Skid Description	Booster/Rotary Piston Pump System
Model Number	MB2001VFD/KT-500D
Number of Skids	4
Motor Capacity	Total: 45 HP, Booster: 15 HP, Rotary Piston Pump: 30 HP
Booster Control	Variable Frequency Drive (VFD) 4-20 mA Signal
VFD Frequency Range	20 to 60 Hz
Operating Pressure (Cavity Helium Vessel)	12 Torr
Booster Operating Speed	2950 RPM (@ 60Hz)
Booster Flow Rate	1180 ACFM (@12 Torr)
Mass Flow Rate	$\approx$ 1.4 g/s
Pressure Sensor Part Number	Edwards Barocel Pressure Transducer W62231611
Pressure Control Signal	0 - 10 V
Pressure Range of Transducer	0 - 100 Torr

Table 3.3.1: Pump skid and pressure sensing specifications.

has a leveling effect by default. Some optimization is needed to regulate liquid helium level throughout a full day accelerator operations. While helium level can change by $\approx$ 20 % during operation it is not ideal. JT and precool valve opening settings have not been found that will regulate a constant helium level during beam operations. Valves have been moved manually during beam operations without tripping the RF but doing this has caused RF trips in the past. The 2K pressure regulation is done via room temperature pumping skids connected to a 9 kW heater on the 2K heat exchanger CAN (HXC) output. The skids are comprised of a roots blower rotary piston pump combination with specifications listed in Table 3.3.1. Four skids are installed for CBETA. The 2K pressure sensor senses pressure through the LHe level stick sensor wire conduit.

When one pump skid is in operation, typically when beam operations are off, the Variable Frequency Drive (VFD) output is 20 Hz. The corresponding helium bath pressure is 6 Torr. At this pressure the cavities are slightly detuned. This condition does impact the RF startup time getting cavities on resonance. One solution is to add load to the helium system with the 2K heater, however using heaters contributes to the lab wide helium load. To avoid using heaters a manual bypass needle valve is installed across the blower input to the blower output thus loading the blower and facilitating constant pressure regulation. The manual valve requires adjustment complicating RF startup. The plan is to add a stepper motor to the valve to mitigate this situation. For the FAT only two blowers were required for stable operation. As the project progresses more pumping capacity is likely needed.

The nominal cryogenic performance illustrated in Fig. 3.3.2 was also within acceptable limits

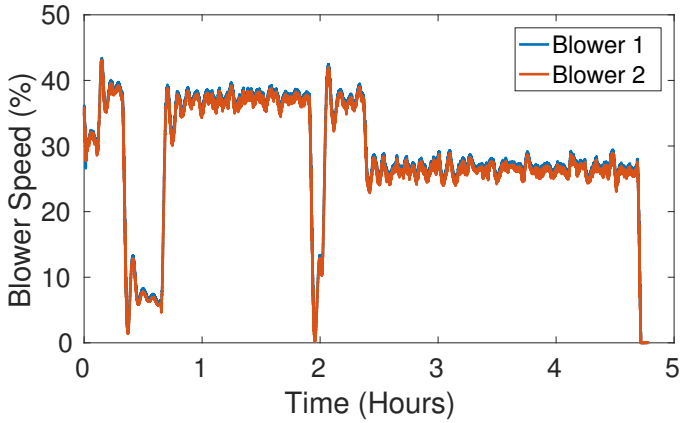

Figure 3.3.2: Blower speeds (percentage of maximum) as functions of time during typical 36 MeV RF operations for the FAT.

with the two blowers connected to the HGRP never exceeding 50 % of maximum speed for nominal energy gain and both reaching 67.5 % at the maximum energy. This indicates that the intrinsic quality factors of the cavities have not degraded from the time of installation and the cryogenic control loops are functioning in an optimum manner.

3.4 Cavity Resonance

The CBETA RF system is synchronized to a master oscillator with a design frequency of 1.3 GHz and all SRF cavities need to be in resonance at this frequency. The tuning angle ϕ_t which is the phase difference between the field signal and the forward power signal is used to measure the detuning δf of the cavities.

$$\delta f = \frac{f_{\text{drive}}}{2Q_L} \tan \phi_t \tag{3.4.1}$$

where Q_L is the loaded quality factor of the cavity and f_{drive} is the clock frequency of the RF system. The cavities are adjusted using a tuner system which mechanically deforms them into resonance i.e. $\delta f = 0$. The tuning range of each cavity is different due to variability in fabrication and need to be measured. In the MLC, three out of the six cavities are mechanically stiffened by welding metal rings (Fig. 3.4.1) on to them which makes them less susceptible to pressure changes in the Helium bath.[25] However at the same time, the extra stiffness leads to a reduced tuning range and in MLC cavity 6, we couldn't tune it to above $1.3\text{GHz} - 80\text{kHz}$. Except for one cavity in the Injector Cryomodule which we detuned far from resonance, we tuned all others to the new master oscillator frequency of 1.2999 GHz and re-optimized the beam optics for operation albeit with some penalty on emittance of the beam.

Apart from the mean resonance frequency, transient deformations can also detune the cavities. One source of time dependent forces is the interaction of the cavity magnetic field with the currents induced in the walls. This leads to Lorentz Force Detuning δf_{LFD} which is a

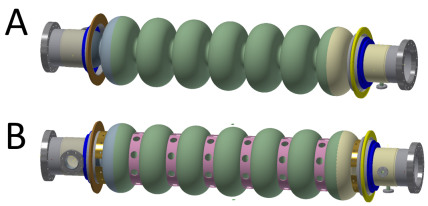

Figure 3.4.1: Main linac cavities used in the CBETA project. A is an unstiffened cavity, while B has stiffening rings welded on to it to make it less susceptible to pressure changes in the Helium bath.

function of electric field E,

$$\delta f_{\mathrm{LFD}} = -K_{\mathrm{LFD}} E^2 \tag{3.4.2}$$

where the minus sign indicates that the resonance frequency decreases with increase in field and K_{LFD} is a constant with a typical value of $1\,\mathrm{Hz/(MV/m)^2}$. Ramping up the accelerating field to the nominal value thus detunes the cavity by over 54 Hz which is more than twice the loaded cavity bandwidth. We use a piezo-electric actuator driven fast tuner to compensate for such transient changes.[23]

Vibration driven microphonics detuning is the most important transient perturbation in the RF system which leads to fluctuating electric field. The maximum forward microwave power P required to sustain an accelerating voltage V under a detuning δf is given by [20]

$$P = \frac{V^2}{8\frac{R}{Q}Q_L}\left\{1 + \left(\frac{2Q_L\delta f}{f}\right)^2\right\} \tag{3.4.3}$$

where, f, $\frac{R}{Q}$ and Q_L are the resonant frequency, shunt resistance and loaded quality factor of the cavity respectively. Using the parameters for the MLC cavities ($Q_L \sim 6 \times 10^7$ and $R/Q \sim 387\,\Omega$), we can estimate that the peak microphonics detuning must be kept below 54 Hz in order to sustain 6 MeV energy gain per cavity using a 5 kW power source. Early measurements showed large peak detuning in un-stiffened cavities leading us to try and identify the source of microphonics.

3.4.1 Microphonics Sources and Mitigation

The microphonics measurements in early 2017 showed strong Fourier modes of vibration near 8 Hz, 40 Hz and 80 Hz as illustrated in figure 3.4.2. Apart from steady vibrations at these frequencies, sudden events resulting in large peak detuning of over 100 Hz were seen in the un-stiffened cavities. In an attempt to find the sources, the microphonics detuning signal was cross-correlated with vibration signatures from various pumps and cryogenic valves attached to the cryomodule and those on the experimental floor. Besides direct mechanical coupling of vibrations through the cavity supports, pressure fluctuations in the liquid helium surrounding the cavity also give rise to microphonics detuning. These transient pressure variations accounted for most of the microphonics in the main linac cavities.

Measurements of microphonics detuning and various cryogenic control parameters showed coincident occurrence of movement of the JT and the precool valve with the large peak de-

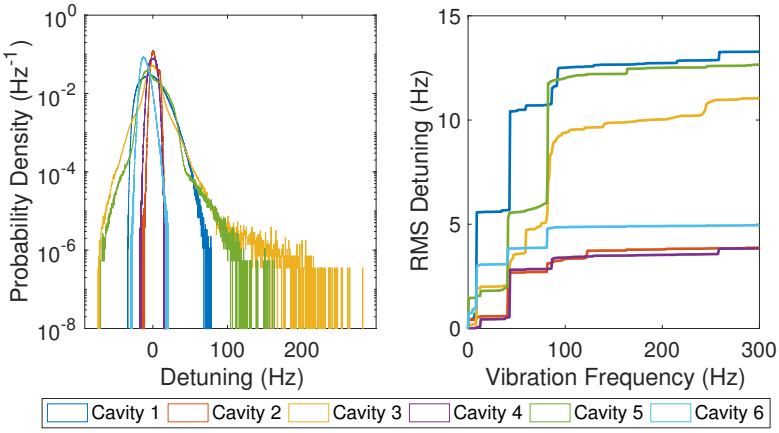

Figure 3.4.2: Microphonics measurements from early 2017, after cryomodule was cooled down to 1.8 K at its final location for CBETA. The left panel shows the histogram of microphonics detuning which indicates the peak values and the right panel indicates the RMS detuning as a function of vibration frequency which indicates frequency content.

tuning events. We verified this effect by measuring detuning after making both valves static. The results of this test are shown in Fig. 3.4.3. In the default configuration, the microphonics histogram shows large peak events which are $\gtrsim$ 200Hz, while the peak microphonics detuning becomes $\sim$ 50Hz with both valves static verifying the proposed mechanism. However, this configuration doesn't allow us to have active control on the liquid Helium level and if the boil off doesn't equal the rate of in-flow from the supply line, then the liquid level in the 2K - 2 phase pipe would steadily run away in either direction. To maintain the Helium level, a heater attached to the 2k - 2 phase pipe is put on a control loop to provide a minimum heat load and boil off Helium when the cavities are not generating enough load and thus stabilize the Helium level. This results in stable operation while limiting the peak detuning to $\sim$ 100Hz a factor of 2 improvement from the original configuration.

The liquid Helium level control using the heater enhances the narrow band 8 Hz vibration line as seen in Fig. 3.4.3. This points to gas flow in the Helium Gas return Pipe (HGRP) as a possible source for the generation of these vibrations. Previous operations data further verified this fact by showing that the line intensity is an increasing function of cavity voltage which determines the dynamic thermal load and hence speed of the external pump. This vibration is possibly an excited eigen-mode of the HGRP and we need further testing to understand the exact mechanism. However as we explain in the next subsection, our active compensation system can effectively reduce its effects on the cavity.

Accelerometer measurements of vibration on the 5 K adjust cryogenic valve stalk yielded significant cross-correlation with the microphonics detuning measurement at 40 Hz and 80 Hz. Figure 3.4.4 shows a schematic of the valve showing the cold region which comes in contact with cold Helium and the warm region which is at room temperature. Delayed heat transfer between the hot and the cold regions trough convection of the Helium gas and conduction through the valve stalk leads to thermo-acoustic oscillations[24] and the resulting pressure

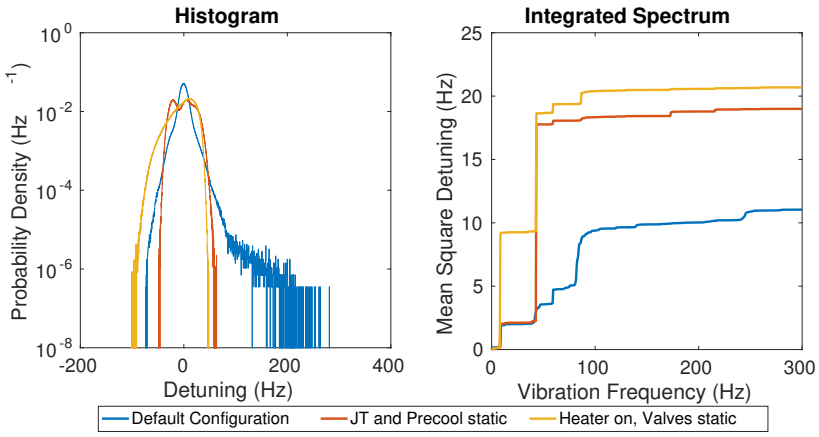

Figure 3.4.3: Influence of valve actuation on microphonics detuning of cavity 3 (unstiffened) showing the detuning histogram on the left panel and the RMS detuning on the right from measurements of duration 800 seconds.

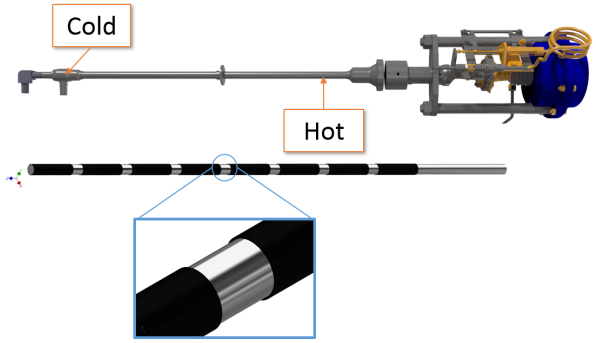

Figure 3.4.4: Cryogenic needle valve used to regulate Helium flow in the cryomodule and the electro-pneumatically actuated valve stem showing attached plastic sleeves.

waves resonate inside the closed space between the valve stem and the valve stalk. We inserted sleeves made of a cryogenic compatible PEEK plastic material on the stem to restrict the gas flow and suppress vibrations.

The microphonics detuning measured just during the Fractional Arc Test after all the modifications is shown in Fig. 3.4.5. The peak detuning on all unstiffened cavities shows a significant reduction from previous results, however a new vibration line can be seen at 59 Hz which wasn't seen during our previous tests. The results from cross-correlation measurements of the microphonics detuning and accelerometer signals from the surface of newly installed beam-pipe and waveguides are shown in Fig. 3.4.6. The results indicate that 59 Hz vibrations from an external source are being mechanically coupled into the cryomodule through the newly installed waveguides. The new source affected cavity 3 the most generating the highest peak detuning ($\sim$ 50Hz) among all others and we used the resonance control system to actively compensate for it.

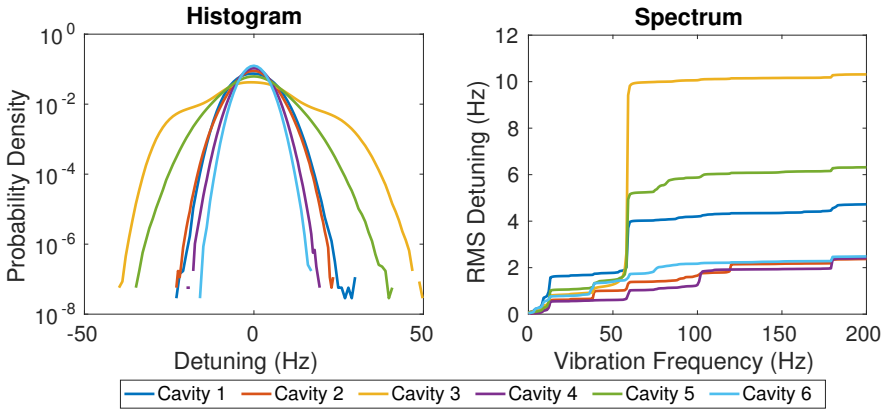

Figure 3.4.5: Microphonics detuning measured for 1 hour on all main linac cavities during the fractional arc test with all cavities running at their design voltage of 6 MV with beam.

3.4.2 Active Resonance Control

Transient changes to the resonant frequency of SRF cavities is the primary constraint on main linac operations of CBETA. Even though the primary method of microphonics reduction is to passively suppress the vibration sources as we discussed in the last section, fast tuners built using piezo-electric actuators are attached to each cavity in order to compensate for LFD and provide an additional method of resonance control which we can use during operations to widen the margin on maximum attainable accelerating voltage on the cavities. In this spirit, we implemented an active microphonics compensation system on the digital signal processor on board the Cornell Low Level radio Frequency (LLRF)[1, 22] to command the actuators. A Proportional-Integral control loop[2] compensates for slow ($\lesssim$ 1Hz) changes in resonant frequency, while a modified narrow band Active Noise Control (ANC) algorithm[3] attenuates higher frequency microphonics detuning. The controller is defined by the equations,

$$u_{\mathrm{pz}}^{\mathrm{ANC}}(t_n) = \sum_m I_m(t_n)\cos(\omega_m t_n) + Q_m(t_n)\sin(\omega_m t_n) \tag{3.4.4a}$$

$$I_m(t_{n+1}) = I_m(t_n) - \mu_m \delta f_{\mathrm{comp}}(t_n)\cos(\omega_m t_n - \phi_m(t_n)) \tag{3.4.4b}$$

$$Q_m(t_{n+1}) = Q_m(t_n) - \mu_m \delta f_{\mathrm{comp}}(t_n)\sin(\omega_m t_n - \phi_m(t_n)) \tag{3.4.4c}$$

$$\phi_m(t_{n+1}) = \phi_m(t_n) - \eta_m \delta f_{\mathrm{comp}}(t_n) \times \Big\{ I_m(t_n)\sin(\omega_m t_n - \phi_m(t_n)) - Q_m(t_n)\cos(\omega_m t_n - \phi_m(t_n)) \Big\}, \tag{3.4.4d}$$

where $u_{\mathrm{pz}}^{\mathrm{ANC}}$ is the actuator command signal which is the output of the algorithm in response to the compensated microphonics detuning δf_{comp} which acts as the input. I_m, Q_m and ϕ_m act as internal states of the controller, while the microphonics frequencies ω_m, gains μ_m and phase adaptation rates η_m are the algorithm parameters fixed by the operator. Figure 3.4.7 shows the results on using this algorithm with $\mu_m = 0.0001$ and $\eta_m = -0.001$ on the 59 Hz vibration line showing a reduction of peak detuning from over 40 Hz to 20 Hz.

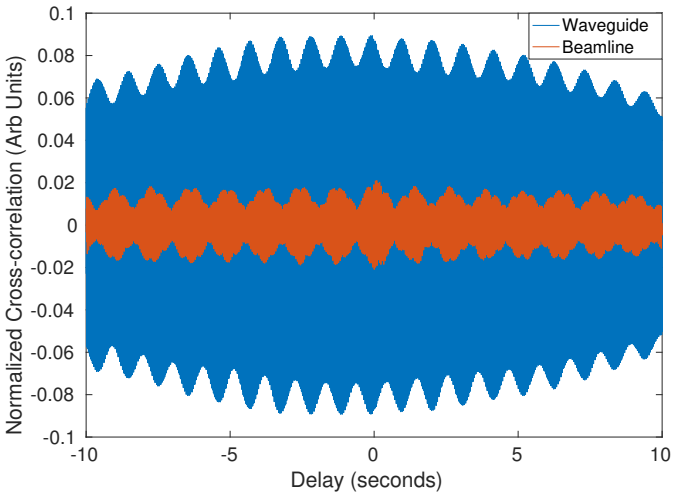

Figure 3.4.6: Cross-correlation between surface acceleration on beampipe and cavity 3 waveguide with microphonics detuning on cavity 3.

3.5 RF Operations

The aim of the Fractional Arc Test was to demonstrate beam optics of a part of CBETA at design energy necessitating the RF commissioning of the MLC to its design field of 6 MeV energy gain per cavity. To this end, each cavity was commissioned separately before the beam could reach design energy. The primary aim of RF commissioning was to achieve long term stability at design field for stable beam operation without spontaneous trips. We further used the MLC to perform an energy scan which tested the upper limits of energy gain.

3.5.1 Individual Cavity RF Commissioning

Figure 3.5.1 presents a simplified schematic of the MLC RF control system, showing the LLRF system, SSA and the SRF cavity with the important signal paths. A proportional integral feedback loop acting independently on the real (in-phase) and imaginary (quadrature) part is used to maintain the complex field phasor near its set point. Rotation matrices programmed into the LLRF provide adjustable phase shifts to various signals including the forward power, reflected power, field and the RF output. The control system commissioning includes setting all these parameters for optimum operation along with calibration of the various signal paths in the system.

Step 0: The calibration of various signals used by the LLRF system involves finding the scales factors which are used to convert the raw Analog to Digital Converter (ADC) readings into physical units including various powers in kW and the energy gain in MeV. We leave the waveguide shorts inserted before the input coupler for convenience and accuracy for this step. To calibrate the forward power channel, we first measure the total attenuation of signal path. We start by measuring the directional coupler with a network analyzer, and then the attenuation of the various cables finally leading into the mixer channel. We also include a splitter in the path which routes the signal into two sets of mixers one for the LLRF and one

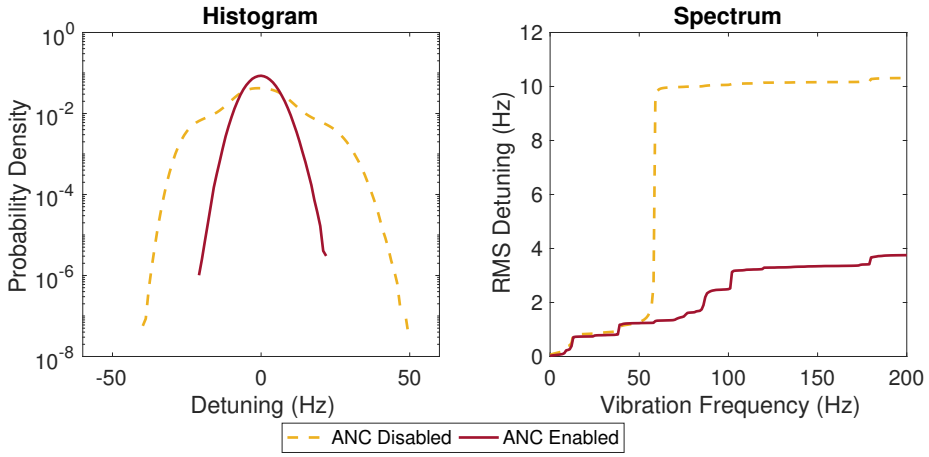

Figure 3.4.7: Microphonics detuning with active noise control disabled and enabled. The histogram shows a factor of 2 reduction in peak detuning while the spectrum shows strong attenuation of the 59 Hz spectral line.

for the diagnostic system. By attaching a calibrated power meter to the diagnostic channel and correcting for the net attenuation we can measure the forward power going into the short when we drive the SSA. Concurrently the LLRF also measures the forward power in terms of ADC counts. Using these measurements we can evaluate the scale parameter K_{fwd} (in kW/count^2) as $K_{fwd} = P/A_{\mathrm{fwd}}^2$, where P is the power measurement from the meter in kW and A_{fwd} is the time averaged un-scaled amplitude of ADC channel 0 from the LLRF system. We follow the same procedure for the reflected power into the SSA from the circulator and use ADC channel 3 for calculating the scale parameter. The power reflected back from the waveguide short while testing must equal the forward power and this is used to calibrate the scale factor for ADC channel 1. We calibrate the field signal (ADC 2) later in step 7 using a beam based procedure.

Step 1: Cavity tuning is the first step towards setting up after cable calibration and we used the stepper motor based slow tuner to obtain resonance at the clock frequency of 1299.9 MHz. We first used a network analyzer to tune the cavity within 10 kHz of the clock frequency at low field while we use the LLRF system in constant power mode (called Klystron Loop in the Cornell LLRF) to fine tune the cavity to within a few Hz of resonance on average. During the tuning process, we try to maximize the field signal which gives us the resonance position as illustrated in Fig. 3.5.2. Microphonics and Lorentz force detuning dynamically change the resonance frequency of the cavity typically by $\lesssim 60$ Hz and as discussed earlier the fast tuner system keeps the transient detuning under control. However, the resonance control system initializes only after the control system successfully establishes the feedback loop at low field and this requires the cavity to be resonant at low accelerating voltages ~ 1 MV. We use a constant forward power of 10 W while tuning the cavities in order to satisfy this criterion.

Step 2: The Digital to Analog Converter (DAC) output used in the LLRF system to drive the vector modulator may have some offset due to manufacturing differences. This leads to some non-zero forward power being injected into the cavity even when the output is set to

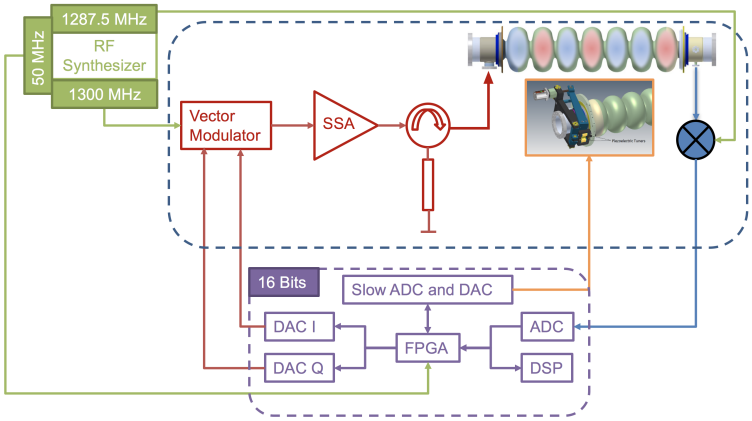

Figure 3.5.1: Simplified diagram of the MLC RF control system showing the various components of the Low Level Radio Frequency (LLRF) system, the RF components including the circulator and the Solid State Amplifier (SSA) and the SRF cavity. The LLRF works at an intermediate frequency (IF) of 12.5 MHz which is phase locked to the 1.3 GHz master oscillator. All RF signals are mixed down to the IF and converted to a phasor for processing in the system, while the output phasor is fed into a vector modulator through a Digital to Analog Converter (DAC) which modulates the carrier frequency of 1.3 GHz.

0 leading to a parasitic field appearing in the cavity even when it is commanded to zero voltage. To account for the offsets, both the in-phase I and the quadrature Q components of the output phasor are shifted by a programmable offset in the LLRF. We measure parasitic forward power as a function of offset as shown in Fig. 3.5.3 setting the optimum value at the position of minimum power.

Step 3: The LLRF system implements various trips which turn off RF power going into the cavity in case of a situation which might damage the RF system. Setting the various trip parameters is an important step in commissioning the cavities. There are three categories of trip parameters which we have to set. The *Klystron (SSA)* trip parameters set the threshold for the maximum power reflected from the circulator into the SSA. The power scale contains a calibration factor while *Max. power* sets the scaled power threshold. The *Power* trip parameters are thresholds on the maximum forward and reflected power, while quench detection relies on a sudden but sustained fractional decrease in reflected power. Finally, we set the *Field* trip parameters which control the maximum field tolerated by the system after step 7. The important trip parameters and their usage are listed in Table 3.5.1.

Step 4: The phase rotation of the field signal due to the cable length between the field probe and the control system influences the stability of the constant field control loop (called Cavity Loop in the Cornell LLRF) and also directly affects the tuning angle measurement used to estimate the detuning. From equation 3.4.1 we can conclude that $\delta f = 0 \implies \phi_t = 0$, and this is used to adjust the field rotation matrix in two steps. We first set the field rotation after manual tuning done in step 1 so that measured tuning angle approximately equals zero. This gives us the rotation value correct to 1-2 degrees. We then observe the average forward power

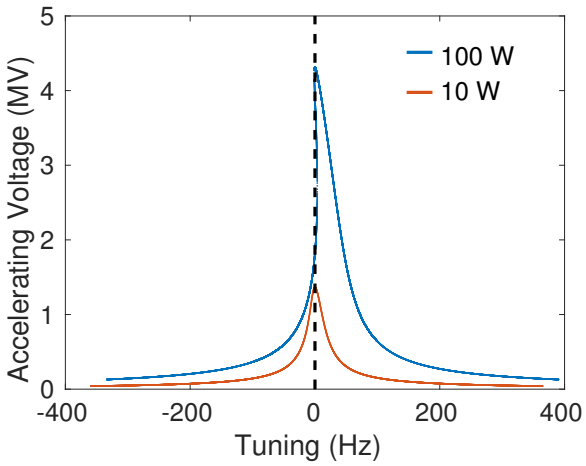

Figure 3.5.2: Theoretical calculation of accelerating voltage as a function of tuner position showing the effect of Lorentz Force Detuning (LFD) on the resonance curve. With a forward power of 10 W, the effects of LFD are negligible, and the field at resonance is ~ 1.3 MV making this the standard tuning procedure. The non-linear hysteresis effects are more noticeable at 100 W when the resonance curve is no longer a single valued function.

required to maintain a stable field in the cavity (Cavity Loop) as a function of the tuning angle ϕ_t set point of the PI feedback loop used in the resonance control system. The position of minimum forward power corresponds to a perfectly tuned cavity, and the phase rotation is adjusted accordingly.

Step 5: Microphonics poses a major constraint on field stability for the MLC cavities which we operate with high Q_L as noted in the previous section. The LLRF system provides a tool to measure the microphonics in the system as shown in Fig. 3.5.4. The LLRF measures the peak forward power and detuning with a time resolution of 10 μsec and 100 μsec respectively. We ensure that the peak microphonics detuning is $\lesssim$ 50Hz for stable operations while the peak power should be less than the maximum output of the SSA connected to the cavities, 5 kW for stiffened and 10 kW for un-stiffened. If deemed necessary, we can use the spectrum measurement to determine the frequencies of strong vibrations in the cryomodule and then activate the ANC algorithm on these sources.

Step 6: Stability of electric field in the RF cavity depends on the proportional and integral gains of the field control loop (cavity Loop). We complete steps 4 and 5 with some default parameters for the control loop, namely with a proportional gain of 3000 and an integral gain of 0. Measurement of standard deviation in field amplitude and phase as a function of the feedback gains is necessary to optimize the performance of the LLRF system. The field stability measurement relies on data sampled at 12.5 MHz by the LLRF system and is processed in matlab. However this wasn't possible due to a bug in the hardware boards we used during the FAT.

Step 7: The energy gain of electrons passing through the cavity and the phase of the electric field when the beam enters the cavity are calibrated using beam measurements which

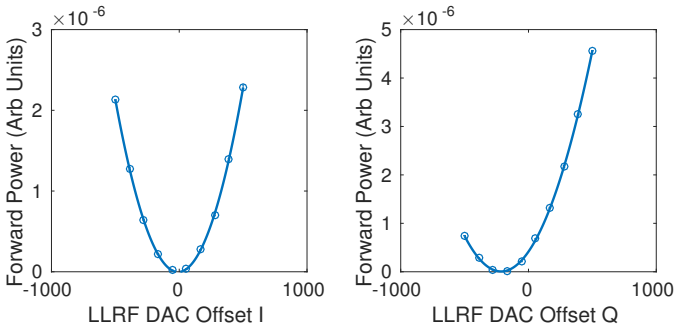

Figure 3.5.3: Forward power as a function of DAC offset in one cavity. We vary the in-phase (I) offset and set it to the position of minimum and then repeat the same for the quadrature (Q) component. The small error bars show that the uncertainties are much smaller than the measurements themselves.

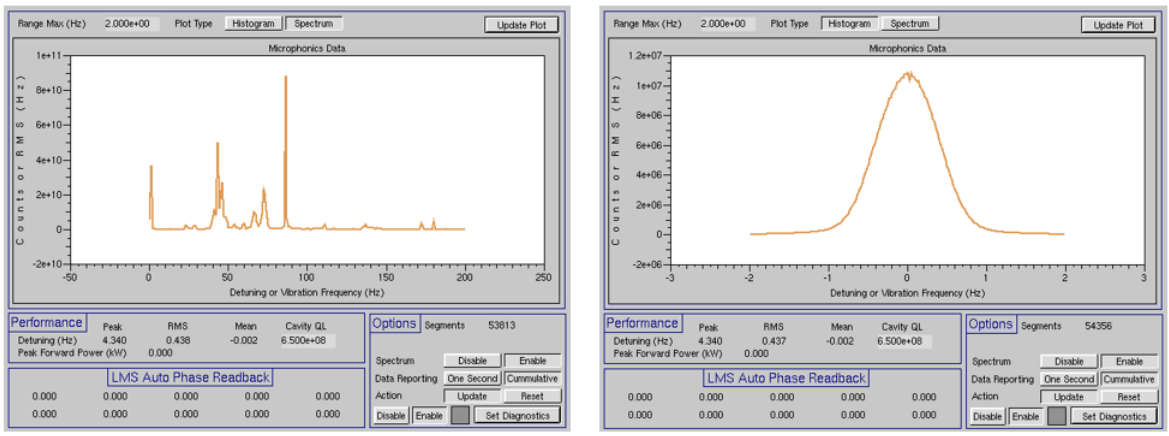

Figure 3.5.4: LLRF control interface showing microphonics diagnostics running on piezo sensor signal. The left panel shows the power spectrum while the right shows the histogram of measured values.

are described in a separate technical note. We update the field trip parameters mentioned in step 3 after we complete this process.

3.5.2 Performance

The performance of the MLC over the course of the FAT can be divided into two distinct periods, one just after RF amplifier testing with the damaged circulators and only five operating SSAs and the second with repaired circulators and all SSAs operational. We achieved the goal of reaching a total energy gain of 36 MeV from the MLC in the first phase regardless of the shortcomings of the RF system including performance limitations and frequent trips. We fully recommissioned all cavities in the second phase and obtained extremely stable performance with the no spontaneous trips and a maximum total energy gain of 53.2 MeV, almost 50% more than the design specification of 36 MeV.

Category	Name	Units	Description
Klystron (SSA)	SSA Refl Power Scale	kW/count^2	Calibration factor for power reflected from the circulator into the SSA.
	Max. power	kW	Maximum power threshold for *Klystron* trip.
Power	Cavity Fwd Power Scale	kW/count^2	Calibration factor for forward power into the cavity.
	Scale Factor Ratio Refl to Fwd		Ratio of reflected and forward power calibration factors.
	Max. Forward Power	kW	Maximum forward power threshold for *Cavity Max Forward* trip.
	Max. Reflected Power	kW	Maximum reflected power threshold for *Cavity Max Reflected* trip.
	Fractional Decrease Trip Level		The fractional decrease threshold for reflected power for a *Cavity Reflected Quench* trip.
	Max. Loop Count	Units of 10μs	Time to wait before declaring a *Cavity Reflected Quench* trip.
Field	Field Square Scale	(kV/count)^2	Calibration factor for square of field.
	Field Amp Sq	(kV)^2	Threshold for *Max Cavity Power* trip.

Table 3.5.1: Trip parameters used in each SRF cavity of the main Linac.

The damage to the circulators and one 10 kW SSA detailed in section 2 prompted us to take extra precautionary steps during the first phase of the FAT. We disabled SSA 5 with the faulty RF slice and consequently cavity 5 was not operational. We fitted multiple temperature sensors on each of the circulators, including one on the tuning screws. Figure 3.5.5 shows some of the temperature measurements with the circulator tuning screw on cavity 3 showing the largest temperature excursions. We shut off the RF system every time the maximum temperature reached 35^o C on circulator 3, further we it fitted with extra water cooling which addressed the overheating problem very effectively. The thermal dependence of the circulator properties manifests itself in the power reflected into the SSAs and we introduced direct monitoring by the LLRF system and set it to trip above a threshold as explained in step 3 of commissioning. Figure 3.5.6 shows the measurements of reflected power showing large values corresponding to the times when the circulator temperatures are higher. These measures protected the RF system from further damage.

Frequent trips interrupted the RF system during this first phase of operations. *Klystron*

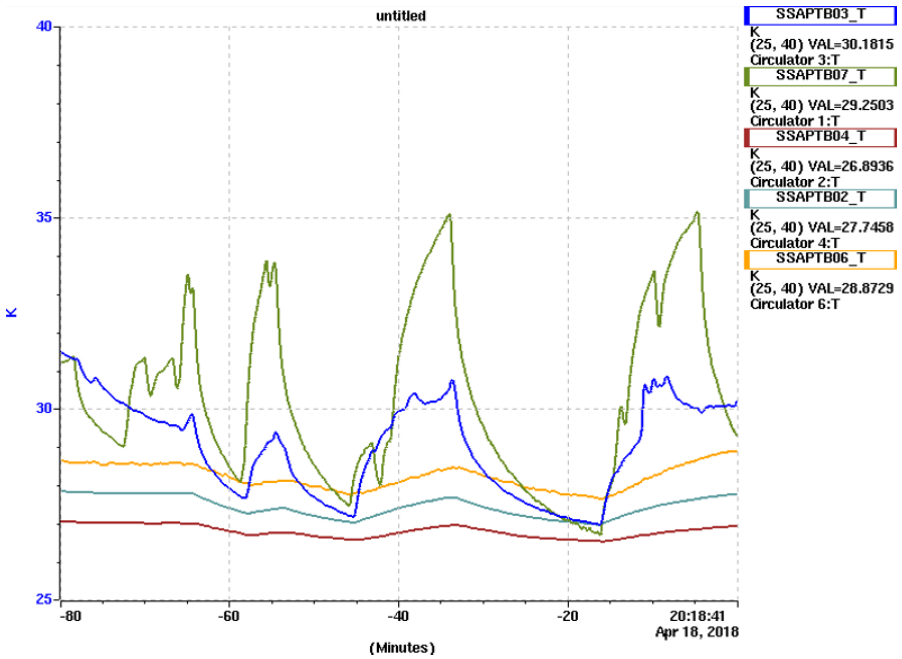

Figure 3.5.5: Circulator tuning screw temperatures as functions of time for five cavities during the first phase of FAT. The big temperature excursions of the green and blue line represent un-stiffened cavities 3 and 1 respectively. We can attribute the large temperatures to higher forward power requirements due to stronger microphonics on these cavities.

trips generated by excessive reflected power on the SSAs were the most common. We reduced the field set points and the proportional gain in response which reduced the forward power generated by the SSAs alleviating the problem. These measures also helped reduce the occurrence of *Max Cavity Power* trips which happen when too much forward power enters the cavity when it is near resonance and lead to spikes in the field. Instabilities in the resonance control system led to *Bad Angle* trips due to cavities suffering a large mechanical transients from the tuner. External factors were mostly responsible for triggering these, including trips in adjacent cavities and instabilities in the piezo-electric drive amplifiers. Most trips during this period could be traced back to the faulty circulators which were repaired towards the end of the FAT.

RF operations after circulator repair were extremely smooth with almost no spontaneous trips with all six MLC cavities, each operating at the design energy of 6 MeV. A summary of the performance of all the MLC cavities is shown in table 3.5.2. The new peak detuning measured during the fractional arc test are smaller in all the un-stiffened cavities leading to lower power consumption when compared to previous commissioning phases. This facilitated driving the MLC to a maximum energy gain of 53.2 MeV during an energy scan experiment. The nominal relative amplitude stability of the accelerating field in the cavities was $\sim 4 \times 10^{-4}$ which is one order larger than the target stability for ERL operations. All the other subsystems including the cryogenic system, SSAs and circulators also worked perfectly as mentioned in

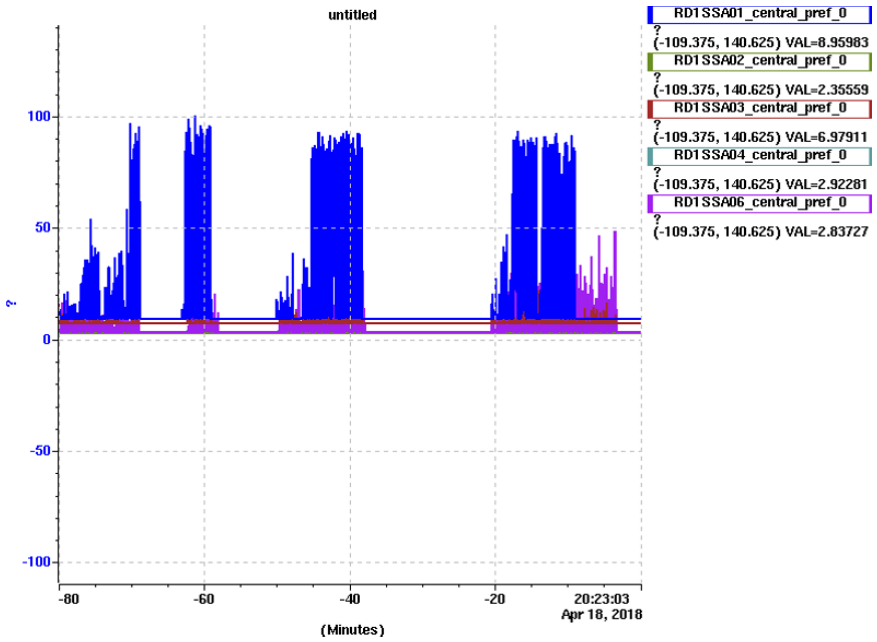

Figure 3.5.6: Power reflected from circulators into SSAs for five cavities as function s of time during the first phase of the FAT. The spikes in reflected power seen on this plot correlates with the temperature excursions seen in figure 3.5.5.

the previous sections.

Besides field stability and the 59 Hz vibrations, RF operations also highlighted some other issues. The most important being the issue of cryomodule alignment, with beam based observations suggesting a vertical offset of as much as 5 mm from the rest of the beamline. Some RF system issues include, on repeating the phase rotation measurement described in step 4, we observed a drift the optimum value by a few degrees on a day to day basis. This effect however disappeared on implementing improved Helium pressure control for the cavities. Secondly, the time averaged tuning angle measurement(Fig. 3.5.7) shows an enhancement of microphonics detuning during the course of the energy scan experiment likely caused by dynamics of the Helium pressure in response to the increased heat load, however we are yet to ascertain the cause. Finally the cavities tend to trip when we command the phase set point to something far from the previous value and is likely caused by inadequate compensation of LFD due to the change in field amplitude when the set point "ramps" from the initial to the final value. We are going to revisit these issues in the next stage of commissioning.

3.6 Conclusion and Outlook

The FAT was the first time we operated the MLC at its design energy for CBETA and all components of the RF system was commissioned before beam operations. We started by testing the six new SSAs supplied by Sigmaphi, three 5 kW units and three 10 kW units which power the stiffened and un-stiffened cavities respectively. After repairing a damaged internal RF module and cable, we tested all of them to full power with satisfactory performance. The

Cavity	Stiffened	Peak Detuning (Hz)		Voltage (MV)	Nominal Amplitude Stability
		Old	New		
1	No	50	30	6 (9.45)	4.0×10^{-4}
2	Yes	20	25	6 (8)	3.9×10^{-4}
3	No	60	50	6 (7.5)	4.0×10^{-4}
4	Yes	20	20	6 (8.5)	4.1×10^{-4}
5	No	(160)	41	6 (8.5)	3.1×10^{-4}
6	Yes	20	18	6 (11.35)	2.9×10^{-4}

Table 3.5.2: RF performance parameters in the second phase of the FAT. The values in parenthesis in the voltage column represent the maximum values reached while 6 MeV is the design value.

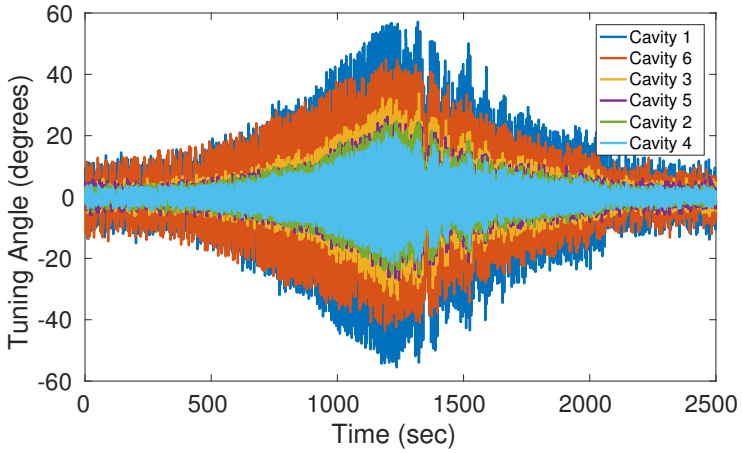

Figure 3.5.7: Time averaged tuning angle $\langle \phi_t \rangle$ as a function of time during the energy scan experiment. Noise enhancement in the plot indicates strong microphonics over all cavities in the cryomodule.

standalone RF tests also exposed a problem with the circulators originating from a high loss polymer being mistakenly used as a spacer between two metal surfaces leading to arcing and consequent damage to the ferrite tiles and pitting of the load surface. This damage translated to thermal runaways on the tuning screws of the loads and severely reduced isolation. However, we went ahead with commissioning for the FAT, starting with cable calibrations all the way up to energy gain measurement and phasing using the beam after which we successfully completed the funding milestone with our limited RF capabilities.

Modifications to the cryogenic system played a significant role in mitigating several strong vibration sources thus reducing the peak power demands of the RF system making it more reliable. We reduced the peak microphonics detuning caused by sudden actuation of cryogenic valves by making them static and used a heater as an alternate route for achieving precise control of the liquid Helium level and vapor pressure in the cryomodule. We further retrofitted the electro-pneumatic 5 K adjust valve with cryogenic compatible plastic sleeves to

inhibit thermo-acoustic instabilities greatly diminishing steady state vibrations of the cavities at 40 Hz and 80 Hz. Finally we also used our active resonance control system to effectively attenuate microphonics detuning at 59 Hz which was being mechanically coupled into cavity 3 (unstiffened) through a waveguide. We were successful in reducing the worst peak detuning to 40 Hz compared to $\gtrsim 100\,\mathrm{Hz}$ seen in the previous stage of commissioning.

After a month of operations, a technician from AFT came to Cornell and repaired the circulator completely mitigating the problems and resulting in very stable RF operations with all cavities. The MLC successfully operated at 6 MeV of energy gain per cavity with a relative amplitude stability of $\sim 4 \times 10^{-4}$ without any spontaneous trips for more than two hours. In an energy scan experiment the total energy gain was successfully raised to 53.2 MeV almost exceeding the nominal by 50 %. The two Helium vapor pumps operated at under 50 % during normal conditions and stayed below 68 % during the energy scan experiment showing optimal operation of the cryogenic system and a nominal intrinsic quality factor for the SRF cavities. This success pave the way to future operations with energy recovery.

We plan to execute a few modifications to the RF system and the cryomodule for the next phase of commissioning. Firstly, we are going to measure the position of the MLC and move it to achieve the best alignment possible. Then, we plan to fully repair the damaged ferrite tiles and the load plates for the circulators to ensure robust isolation for the SSAs. We are going to setup and troubleshoot the MODBUS communication to all the SSAs. To further reduce vibrations we are going to fit the other cryogenic valves with the same plastic sleeves and damp the vibrations coupling in through the waveguide. We are going to automate the bypass valve on the blowers to effectively put a dummy load and help in Helium level control. We are going to optimize for RF field stability and update the LLRF software to have more sophisticated field and resonance control algorithms to make it more robust and reduce spontaneous trips. Finally, we are going to automate the cavity commissioning steps as much as possible and have a new simplified graphics interface to help troubleshoot the system semi-automatically. Hopefully, these will prepare us for 1 mA multi-turn operation with energy recovery.

Bibliography

[1] A Neumann, W Anders, R. G. J. K. O. K. S. B. J. D. R. K. M. L. C. S. [2011]. Cw measurements of cornell llrf system at hobicat, *SRF Workshop* . MOPO67.

[2] Banerjee, N. et al. [2017]. Microphonics Studies of the CBETA Linac Cryomodules, *Proc. of International Particle Accelerator Conference (IPAC'17), Copenhagen, Denmark, 1419 May, 2017*, number 8 in *International Particle Accelerator Conference*, JACoW, Geneva, Switzerland, pp. 1138–1141. https://doi.org/10.18429/JACoW-IPAC2017-MOPVA122. **URL:** *http://jacow.org/ipac2017/papers/mopva122.pdf*

[3] Banerjee, N. et al. [2018]. Microphonics Suppression in the CBETA Linac Cryomodules, number 9 in *International Particle Accelerator Conference*, JACoW, Vancouver, Canada.

[4] Dunham, B., Barley, J., Bartnik, A., Bazarov, I., Cultrera, L., Dobbins, J., Hoffstaetter, G., Johnson, B., Kaplan, R., Karkare, S., Kostroun, V., Li, Y., Liepe, M., Liu, X., Loehl, F., Maxson, J., Quigley, P., Reilly, J., Rice, D., Sabol, D., Smith, E., Smolenski,

K., Tigner, M., Vesherevich, V., Widger, D. and Zhao, Z. [2013]. Record high-average current from a high-brightness photoinjector, *Applied Physics Letters* **102**(3): 034105.
URL: *https://doi.org/10.1063/1.4789395*

[5] Eichhorn, R. et al. [2014]. Cornell's Main Linac Cryomodule for the Energy Recovery Linac Project, *Proceedings, 5th International Particle Accelerator Conference (IPAC 2014): Dresden, Germany, June 15-20, 2014*, p. WEPRI061.
URL: *http://jacow.org/IPAC2014/papers/wepri061.pdf*

[6] Eichhorn, R. et al. [2015a]. Complection of the Cornell High Q CW Full Linac Cryomodule, *Proceedings, 6th International Particle Accelerator Conference (IPAC 2015): Richmond, Virginia, USA, May 3-8, 2015*, p. WEPTY069.
URL: *http://accelconf.web.cern.ch/AccelConf/IPAC2015/papers/wepty069.pdf*

[7] Eichhorn, R. et al. [2015b]. The Cornell Main Linac Cryomodule: A Full Scale, High Q Accelerator Module for cw Application, *Proceedings, International Cryogenic Engineering Conference and International Cryogenic Materials Conference 2014 (ICEC 25 ICMC 2014): Enschede, The Netherlands, July 7-11, 2014*, Vol. 67, pp. 785–790.

[8] Eichhorn, R. et al. [2016]. First Cool-down of the Cornell ERL Main Linac Cryo-Module, *Proceedings, 7th International Particle Accelerator Conference (IPAC 2016): Busan, Korea, May 8-13, 2016*, p. WEPMR020.
URL: *http://inspirehep.net/record/1470183/files/wepmr020.pdf*

[9] Furuta, F. et al. [2015]. Performance of the Cornell ERL Main Linac Prototype Cryomodule, *Proceedings, 17th International Conference on RF Superconductivity (SRF2015): Whistler, Canada, September 13-18, 2015*, p. FRAA04.
URL: *http://inspirehep.net/record/1482260/files/fraa04.pdf*

[10] Furuta, F. et al. [2016]. ERL Main Linac Cryomodule Cavity Performance and Effect of Thermal Cycling, *Proceedings, 7th International Particle Accelerator Conference (IPAC 2016): Busan, Korea, May 8-13, 2016*, p. WEPMR022.
URL: *http://inspirehep.net/record/1470185/files/wepmr022.pdf*

[11] Furuta, F. et al. [2017a]. ERL Cryomodule Testing and Beam Capabilities, *Proceedings, 8th International Particle Accelerator Conference (IPAC 2017): Copenhagen, Denmark, May 14-19, 2017*, p. WEPIK036.
URL: *http://inspirehep.net/record/1627164/files/wepik036.pdf*

[12] Furuta, F. et al. [2017b]. Performance of the Novel Cornell ERL Main Linac Prototype Cryomodule, *Proceedings, 28th International Linear Accelerator Conference (LINAC16): East Lansing, Michigan, September 25-30, 2016*, p. TUPLR011.
URL: *http://inspirehep.net/record/1633195/files/tuplr011.pdf*

[13] Furuta, F. et al. [2018]. High-efficiency, High-current Optimized Main-linac ERL Cryomodule, *Proceedings, 18th International Conference on RF Superconductivity (SRF2017): Lanzhou, China, July 17-21, 2017*, p. FRXAA02.
URL: *http://inspirehep.net/record/1669554/files/frxaa02.pdf*

[14] Ge, M., Banerjee, N., Dobbins, J., Eichhorn, R., Furuta, F., Hoffstaetter, G., Liepe, M., Quigley, P., Sears, J. and Veshcherevich, V. [2017]. Measurements and Analysis of Cavity Microphonics and Frequency Control in the Cornell ERL Main Linac Prototype Cryomodule, *Proceedings, 28th International Linear Accelerator Conference (LINAC16): East Lansing, Michigan, September 25-30, 2016*, p. TUPLR010.
URL: *http://inspirehep.net/record/1633194/files/tuplr010.pdf*

[15] Hartill, D. L., Hoffstaetter, G. H., Liepe, M., Posen, S., Quigley, P. and Veshcherevich, V. [2011]. Experience with the Cornell ERL Injector SRF Cryomodule during High Beam Current Operation, *Particle accelerator. Proceedings, 2nd International Conference, IPAC 2011, San Sebastian, Spain, September 4-9, 2011*, Vol. C110904, pp. 35–37.

[16] He, Y., Hoffstaetter, G. H., Liepe, M., Tigner, M. and Smith, E. N. [2012]. Cryogenic Distribution System for the Proposed Cornell ERL Main Linac, *Proceedings, 3rd International Conference on Particle accelerator (IPAC 2012): New Orleans, USA, May 2-25, 2012*, Vol. C1205201, pp. 619–621.

[17] Hoffstaetter, G. H., Liepe, M., Posen, S., Quigley, P. and Veshcherevich, V. [2012]. High Current Operation of the Cornell ERL Superconducting RF Injector Cryomodule, *Proceedings, 3rd International Conference on Particle accelerator (IPAC 2012): New Orleans, USA, May 2-25, 2012*, Vol. C1205201, pp. 2378–2380.

[18] Hoffstaetter, G. H. et al. [2017a]. CBETA Design Report, Cornell-BNL ERL Test Accelerator, *Technical report*.

[19] Hoffstaetter, G. et al. [2017b]. CBETA: The Cornell/BNL 4-Turn ERL with FFAG Return Arcs for eRHIC Prototyping, *Proceedings, 28th International Linear Accelerator Conference (LINAC16): East Lansing, Michigan, September 25-30, 2016*, p. TUOP02.
URL: *http://inspirehep.net/record/1633164/files/tuop02.pdf*

[20] Liepe, M. and Belomestnykh, S. [2003]. RF Parameter and Field Stability Requirements for the Cornell ERL Prototype, *Particle accelerator. Proceedings, Conference, PAC 2003, Portland, USA, May 12-16, 2003*, Vol. C030512, p. 1329.

[21] Liepe, M., Belomestnykh, S., Chojnacki, E., Conway, Z., Medjidzade, V., Padamsee, H., Quigley, P., Sears, J., Shemelin, V. and Veshcherevich, V. [2010]. SRF Experience with the Cornell High-Current ERL Injector Prototype, *Particle accelerator. Proceedings, 23rd Conference, PAC'09, Vancouver, Canada, May 4-8, 2009*, p. TU3RAI01.
URL: *http://accelconf.web.cern.ch/AccelConf/PAC2009/papers/tu3rai01.pdf*

[22] Liepe, M., Belomestnykh, S., Dobbins, J., Kaplan, R., Strohman, C. and Stuhl, B. [2005]. Experience with the new digital rf control system at the cesr storage ring, *Proceedings of the 2005 Particle Accelerator Conference*, pp. 2592–2594.

[23] Liepe, M. and Posen, S. [2012]. Measurement of the Mechanical Properties of Superconducting Cavities During Operation, *Proceedings, 3rd International Conference on Particle accelerator (IPAC 2012): New Orleans, USA, May 2-25, 2012*, Vol. C1205201, pp. 2399–2401.

[24] Luck, H. and Trepp, C. [1992]. Thermoacoustic oscillations in cryogenics. part 1: basic theory and experimental verification, *Cryogenics* **32**(8): 690 – 697.
URL: *http://www.sciencedirect.com/science/article/pii/001122759290277H*

[25] Posen, S. and Liepe, M. [2012]. Mechanical optimization of superconducting cavities in continuous wave operation, *Phys. Rev. ST Accel. Beams* **15**: 022002.

[26] Trbojevic, D. et al. [2017]. CBETA - Cornell University Brookhaven National Laboratory Electron Energy Recovery Test Accelerator, *Proceedings, 8th International Particle Accelerator Conference (IPAC 2017): Copenhagen, Denmark, May 14-19, 2017*, p. TUOCB3.
URL: *http://inspirehep.net/record/1626821/files/tuocb3.pdf*

4 Conclusions

The CBETA fractional arc test provided invaluable experience testing and commissioning many of the most critical subsystems to the CBETA. Full beam commissioning of the MLC yielded beam energies up to roughly 60 MeV, nearly a factor of 1.6 times the 36 MeV necessary for the CBETA design. The MLC commissioning required development of many important measurement procedures including a method for cavity energy gain calibration using BPM time of arrival. Together with MLC commissioning, the CBETA splitter line and permanent magnet BPM systems were commissioned with beam and procedures for non-linearity correction quantified for the splitter BPMs. Beam-based measurements taken during the FAT provide evidence that the splitter magnets produced by Elytt are not only functional, but may meet their specification within the error estimates of the measurement procedure (further analysis is forthcoming). Similarly, the successful passage of the beam through the first permanent magnet prototype girder and measurement of the tune shifts per cell represents another critical milestone for the CBETA project. The measurement techniques used here to measure the tunes and determine the BPM offsets should prove extremely useful for commissioning the full permanent return loop. The FAT also allowed for evaluation and development of the CBETA-V online modeling, and ultimately demonstrating its usefulness as a tool for not only displaying useful physics data to operators in real time, but also for debugging and testing measurement procedures before putting them to use in the real machine.

The results of the FAT highlight several important issues that require addressing prior to future beam commissioning and operations. Measurement of the MLC cavity offsets of roughly 5.5 mm (on average) represents a particularly important, if surprising, example. Others include difficulty establishing a reproducible good match of the injector beam into the MLC and splitter line, lack of an automated MLC cavity phasing procedure, the inability currently to quantify the FA style BPM non-linearity, and lack of development for diagnostic procedures (other than beam profiles on viewscreens) to verify the match *after* the linac. Additionally, while we did develop and test a measurement method for determining the corrector BPM response matrix throughout the machine, we did not substantially test the orbit correction software under development for CBETA. Fortunately, with the help of the CBETA-V online model, this work has been able to continue past the end of the FAT experimental period, with promising initial results using Single Value Decomposition (SVD) [1]. We have not at this time fully accounted for the discrepancy between the quad settings giving the best fit to the dispersion in the permanent magnet arc in measurement and in the BMAD FAT model. Measurements of the tunes via induced betatron oscillations around the periodic orbit suggest an overall energy scale factor accounts for the discrepancy between the measured and simulated tunes as a function of beam energy. This could arise from an unknown systematic discrepancy between the 3D field maps for the permanent magnets and the fields in the magnets themselves or from an error in our energy calibration.

Significant effort is currently underway to address many of these issues: offline analysis of

beam-based calibration data for the splitter magnets continues, as does orbit correction software development. In addition to the direct measurement of the BPM non-linearity described in this work, 3D RF simulations of the splitter/FA BPM designs have been planned. Additionally, we plan to explore new injector machine settings via MOGA optimziation, as well as investigating methods for verifying the match after the linac. Perhaps most importantly, the entrance and exit beamlines to the MLC as well as the cryostat itself are currently being surveyed with the goal of centering the MLC for operation with the full return loop. Given the demonstrated usefulness of the CBETA-V online model, significant development of the software is ongoing, and we have begun to use the 42 MeV energy recovery lattice in the model. With this work and more we hope to build on the results achieved during the CBETA FAT as we move forward to the final completion of CBETA construction and beam commissioning.

Bibliography

[1] Nunez-delPrado, A. and C. Gulliford. *CBETA-V: Advanced Online Simulation Tools for the CBETA Machine*. Technical report, CLASSE, Cornell University (2018).